Structural Engineering and Mechanics, *Vol. 86, No. 3 (2023) 291-309*
https://doi.org/10.12989/sem.2023.86.3.291

Formulation and evaluation a finite element model for free vibration and buckling behaviours of functionally graded porous (FGP) beams

Abdelhak Mesbah[1a], Zakaria Belabed*[2,3], Khaled Amara[4], Abdelouahed Tounsi[2,5,6], Abdelmoumen A. Bousahla[7] and Fouad Bourada[2,8]

[1]*Smart Structures Laboratory, Faculty of Science & Technology, Civil Engineering Department, University of Ain Témouchent, Po Box 284, 46000 Ain-Temouchent, Algeria*
[2]*Material and Hydrology Laboratory, Faculty of Technology, Civil Engineering Department, University of Sidi Bel Abbes, Algeria*
[3]*Department of Technology, Institute of Science and Technology, Naama University Center, BP 66, 45000 Naama, Algeria*
[4]*Engineering and Sustainable Development Laboratory, University of Ain Temouchent, Ain Temouchent 46000, Algeria*
[5]*Department of Civil and Environmental Engineering, King Fahd University of Petroleum & Minerals, 31261 Dhahran, Eastern Province, Saudi Arabia*
[6]*FL (Yonsei Frontier Lab), Yonsei University, Seoul, Korea*
[7]*Laboratoire de Modélisation et Simulation Multi-échelle, University of Sidi Bel Abbés, Algeria*
[8]*Département des Sciences et de la Technologie, Université de Tissemsilt, BP 38004 Ben Hamouda, Algérie*

(*Received August 27, 2021, Revised February 26, 2023, Accepted February 27, 2023*)

Abstract. This paper addresses the finite element modeling of functionally graded porous (FGP) beams for free vibration and buckling behaviour cases. The formulated finite element is based on simple and efficient higher order shear deformation theory. The key feature of this formulation is that it deals with Euler-Bernoulli beam theory with only three unknowns without requiring any shear correction factor. In fact, the presented two-noded beam element has three degrees of freedom per node, and the discrete model guarantees the interelement continuity by using both C^0 and C^1 continuities for the displacement field and its first derivative shape functions, respectively. The weak form of the governing equations is obtained from the Hamilton principle of FGP beams to generate the elementary stiffness, geometric, and mass matrices. By deploying the isoparametric coordinate system, the derived elementary matrices are computed using the Gauss quadrature rule. To overcome the shear-locking phenomenon, the reduced integration technique is used for the shear strain energy. Furthermore, the effect of porosity distribution patterns on the free vibration and buckling behaviours of porous functionally graded beams in various parameters is investigated. The obtained results extend and improve those predicted previously by alternative existing theories, in which significant parameters such as material distribution, geometrical configuration, boundary conditions, and porosity distributions are considered and discussed in detailed numerical comparisons. Determining the impacts of these parameters on natural frequencies and critical buckling loads play an essential role in the manufacturing process of such materials and their related mechanical modeling in aerospace, nuclear, civil, and other structures.

Keywords: buckling; finite element method; free vibration; functionally graded porous (FGP) beams; shear deformation beam theory; two-noded isoparametric finite element

1. Introduction

In recent years, functionally graded materials (FGMs) have been recognized as an enhanced class of composite materials that have been attracting considerable interest in a large array of applied engineering disciplines, especially in aerospace, automotive, nuclear, biomedical, and civil engineering structures (Ebrahimi and Zia 2015, Madenci and Özütok 2017, Ebrahimi *et al.* 2018, Madenci 2019, Punera and Kant 2019, Madenci and Özütok 2020, Civalek and Avcar 2020, Belabed *et al.* 2021, Slimani *et al.* 2021, Vinyas *et al.* 2021). The main reason for using FGMs in various applications returns to their excellent mechanical properties, such as optimum strength/weight ratio, high stiffness, durability, and recent engineering design preferences (Chen *et al.* 2021). A typical FGM is founded on a continuous and smooth mixture of both metallic and ceramic materials through the thickness coordinate; this gradual change in properties eliminates several problems over conventional composites, including exceptionally high interlaminar stress concentrations and delamination. A practical factor associated with functionally graded materials is the porosity that can be engendered into the microstructure of these materials. Many researchers have identified porosity as a valuable parameter for special structural performance requirements such as thermal conductivity reduction, low cost of FGM manufacturing, lightweight structures, noise reduction, and significant energy-absorbing capability via impact loads (Smith *et al.* 2012, Zhao 2012, He *et al.* 2017, Liu *et al.* 2018, Xiao *et al.* 2019, Ebrahimi *et al.* 2019, Hamed *et al.* 2019, Xu *et al.* 2020, Cuong-Le *et al.* 2020a, Cuong-Le *et al.* 2020b).

*Corresponding author, Ph.D.
E-mail: belabed.zak@gmail.com
[a]Ph.D. Student
E-mail: abdelhak.mesbah@univ-temouchent.edu.dz

ISSN: 1225-4568 (Print), 1598-6217 (Online)

Thus, the effect of porosity on mechanical structural response has received an increase attention in several recent studies. Chen *et al.* (2015) proposed a parametric study to investigate the effect of porosity on elastic buckling and static bending of functionally graded porous Timoshenko beams. Kitipornchai *et al.* (2016) applied the Ritz method to predict the free vibration and elastic buckling responses of functionally graded porous beams reinforced by graphene platelets using the Timoshenko beam theory. Chen *et al.* (2016) used the Timoshenko beam theory and the Ritz method to investigate the effect of porosity distributions and boundary conditions on free and forced vibration analysis of porous functionally graded beams. Galeban *et al.* (2016) presented a free vibration study of functionally graded beams with porosities based on the Euler-Bernoulli theory. To investigate the static behaviour of laminated composite beams, Özütok and Madenci (2017) proposed a new mixed finite element model based on an efficient higher-order shear deformation theory. Mirjavadi *et al.* (2017) investigated the thermal vibration of two-dimensional porous, functionally graded nanobeams using the Timoshenko beam theory and the generalized differential quadrature method. Eltaher *et al.* (2018) adopted a modified porosity model to study the static bending and free vibration of porous functionally graded nanobeams according to the Euler-Bernoulli beam theory. Mirjavadi *et al.* (2018) have resolved the nonlinear vibration and buckling problems of Euler-Bernoulli functionally graded porous nanoscale beams by applying the generalized differential quadrature method. Fazzolari (2018) formulated various higher-order beam theories to study the vibration and stability analysis of porous functionally graded sandwich beams resting on elastic foundations, and using the Ritz method solution. In conjunction with the third-order shear deformation beam theory with the Chebyshev collocation approach, Wattanasakulpong *et al.* (2018) modelled the vibrational behaviour of functionally graded porous beams with different general boundary conditions and porosity distributions. Wu *et al.* (2018) performed a finite element analysis on the dynamic analysis of functionally graded porous structures by considering both Euler-Bernoulli and Timoshenko beam theories. Anirudh *et al.* (2019) have devoted a comprehensive analysis to studying the bending, buckling, and vibration behaviours of curved porous graphene-reinforced beams by using a higher-order finite element beam model. Gao *et al.* (2019) used Timoshenko's beam theory and the method of differential quadrature to investigate the dynamic characteristics of porous functionally graded beams with material uncertainties. Liu *et al.* (2019) applied the porosity effects on buckling analysis of porous functionally graded beams in thermal environments using a high-order sinusoidal shear deformation beam theory and the physical neutral concept. Bourada *et al.* (2019) presented a refined higher-order beam theory for dynamic investigations of porous functionally graded beams. Jamshidi *et al.* (2019) used the generalized differential quadrature method and Timoshenko beam theory for porosity optimization of two-dimensional functionally graded porous beams. Al-Maliki *et al.* (2019) evaluated a finite element model for free vibration analysis of porous metal foam nanobeams based on refined shear beam theory. Akbas (2018) presented a twelve-node plane finite element to analyze the effects of both material and porosity parameters on the forced response of functionally graded porous deep beams. To investigate the mechanical behaviours of thick functionally graded porous beams, Fang *et al.* (2019) proposed a quasi-3D beam theory with isogeometric analysis. Zhao *et al.* (2019) suggested a modified series solution to demonstrate the effect of different boundary conditions and porosity coefficients on free vibration analysis of both curved and straight functionally graded porous Timoshenko beams. Fahsi *et al.* (2019) assessed the implications of porosity and elastic foundation parameters on the mechanical response of functionally graded porous beams forming a new Quasi-3D beam theory. Qin *et al.* (2020) discussed the effect of arbitrary boundary conditions and different types of porosity distributions on both the free and forced vibration responses of porous functionally graded beams. In this research, they have used a higher-order shear deformation beam theory in conjunction with the Jacobi-Ritz approach to solving the governing equations. Wu *et al.* (2020) presented a comprehensive state of the art on various mechanical behaviours of functionally graded porous structures. Akbas *et al.* (2020) considered the viscoelastic support effect and proposed a 2D plane finite element formulation to determine the dynamic response of functionally graded porous multilayer thick beams. An overall review of the free vibration behaviour of both perfect and imperfect functionally graded beams is presented by Zahedinejad *et al.* (2020). Jena *et al.* (2020) discussed the free vibration analysis of a functionally graded porous beam embedded in the Kerr foundation using the shifted Chebyshev polynomials, Rayleigh-Ritz method, and Navier's technique. Derikvand *et al.* (2021) employed a refined beam theory to analyze the mechanical buckling of functionally graded thick porous core sandwich beams via the differential transform method. A dynamic analysis was carried out for functionally graded porous beams using the complementary functions method based on the Timoshenko beam theory by Noori *et al.* (2021). The investigation by Akbas (2021) showed the influence of porosity distribution and porosity coefficients on the dynamic responses of axially functionally graded porous beams over moving loads using the Ritz method. Madenci (2021a) performed a vibrational analysis for carbon nanotube-reinforced nanocomposite beams using variational approaches. Madenci (2021b) developed a mixed finite element model to assess both the static and dynamic responses of functionally graded beams. Alnujaie *et al.* (2021) studied damped forced vibration of functionally graded beams with porosity under sinusoidal harmonic point load using a twelve-node 2D plane element.

Moreover, the commonly used theories proved their ability to simulate the mechanical response of FGP beams with interesting results. In contrast to Euler-Bernoulli and Timoshenko beam theories, the higher-order shear beam theories are more accurate and efficient, and the researchers conceived them to analyze the mechanical behaviour of thick beams. In addition, many advanced methods have

been developed to overcome the limitations of analytical methods to solve a variety of FGP beam simulations. Rather than conventional approximate approaches such as the Ritz method, generalized differential quadrature, isogeometric analysis, and Chebyshev collocation method, where each method ensures different merits regarding implementation, a high level of exactness, and stability, the finite element method is considered a robust, reliable, and efficient method and is generally employed in advanced structural design codes.

In this paper, a higher-order finite element model is formulated and evaluated to investigate the porosity distribution effects on the free vibration and buckling analysis of FGP beams. Unlike other higher-order shear deformation beam theories, that generate a host of unknowns, the present theory has only three unknowns and provides an easily implementable formulation for the finite element method (with three degrees of freedom per node). The formulated element features two nodes and three degrees of freedom per node (u, ϕ_x, and$w$) expressed in isoparametric coordinates suitable for Gauss quadrature and the interelement continuity requirement is satisfied, the derived stiffness, geometric and mass matrices result from a weak form of the governing equations. This beam element is free of shear locking by applying the reduced integration technique to evaluate the shear strain energy. A detailed numerical comparison is performed to validate and evaluate the efficiency and simplicity of the proposed formulation; it appears to be in excellent agreement with the above-mentioned theories, the effect of porosity on the free vibration and buckling problems is exploited by using various distribution models. Additionally, the present element is simple to use, retains important physical characteristics, and is more amenable to simulating the mechanical behaviour of FGP beams. Finally, researchers still focus on the proposed element to investigate other FG structures problems (Mehar and Panda 2019, Bendaho *et al.* 2019, Wang *et al.* 2017, Yaylaci *et al.* 2020, Eltaher *et al.* 2020, Selmi 2020, Madenci and Gülcü 2020).

2. Theoretical formulation

2.1 Geometrical configuration

Consider a straight beam with uniform thickness h referring to a rectangular Cartesian coordinates (x,y and z). The both top and bottom faces of the beam are at $z = \pm h/2$ respectively.

2.2 Material properties of FGP beams

The material properties of the FGP beam are assumed to vary smoothly and gradually through the beam thickness. The imperfection of the pores allows the distribution function to be included in the materials constituting the FGP beam, there are various porosity distributions used to evaluate the mechanical properties of FGP structures. The Young's modulus, shear modulus, and mass density vary across the beam thickness according to the graded non-uniform porosity that can be stated in the form:

Porosity distribution *Type-I*

$$E(z) = E_1\left[1 - e_0\cos\left(\frac{\pi z}{h}\right)\right] \tag{1a}$$

$$G(z) = G_1\left[1 - e_0\cos\left(\frac{\pi z}{h}\right)\right] \tag{1b}$$

$$\rho(z) = \rho_1\left[1 - e_m\cos\left(\frac{\pi z}{h}\right)\right] \tag{1c}$$

and porosity distribution *Type-II*

$$E(z) = E_1\left[1 - e_0\cos\left(\frac{\pi z}{2h} + \frac{\pi}{4}\right)\right] \tag{2a}$$

$$G(z) = G_1\left[1 - e_0\cos\left(\frac{\pi z}{2h} + \frac{\pi}{4}\right)\right] \tag{2b}$$

$$\rho(z) = \rho_1\left[1 - e_m\cos\left(\frac{\pi z}{2h} + \frac{\pi}{4}\right)\right] \tag{2c}$$

and

$$e_m = 1 - \sqrt{1 - e_0} \tag{3}$$

where (E_1,G_1 and ρ_1) and (E_0,G_0 and ρ_0) are the maximum and minimum Young's modulus, shear modulus, mass density of the FGP beam, respectively. e_0 and e_m present the porosity coefficients of the relative Young's modulus and density of FGP beam.

The volume fraction of inclusions (both ceramic and metal) and the porosity parameter are also used to describe other porosity distributions. Among those, the effective material properties of FG beams accounting for porosities are computed by the following models:

Porosity distribution *Type-III*

$$E(z) = (E_c - E_m)V_c(z) + E_m - \frac{e_0}{2}(E_c + E_m) \tag{4a}$$

$$\rho(z) = (\rho_c - \rho_m)V_c(z) + \rho_m - \frac{e_0}{2}(\rho_c + \rho_m) \tag{4b}$$

Porosity distribution *Type-IV*

$$E(z) = (E_c - E_m)V_c(z) + E_m - \frac{e_0}{2}(E_c + E_m)\left(1 - \frac{2|z|}{h}\right) \tag{5a}$$

$$\rho(z) = (\rho_c - \rho_m)V_c(z) + \rho_m - \frac{e_0}{2}(\rho_c + \rho_m)\left(1 - \frac{2|z|}{h}\right) \tag{5b}$$

The power-law distribution is used to evaluate the material properties of FG beams. In this study, the volume fraction can be stated in the form: (Avcar 2019, Hadji 2020, and Mehala *et al.* 2018)

$$V_c(z) = \left(\frac{2z + h}{2h}\right)^p \tag{6}$$

Here; p is the volume fraction index ($0 \le p \le +\infty$), which dictates the material variation profile through the thickness, and the subscripts *m* and *c* represent the metallic and ceramic constituents respectively and the related Poisson's ratio is assumed to be constant for convenience.

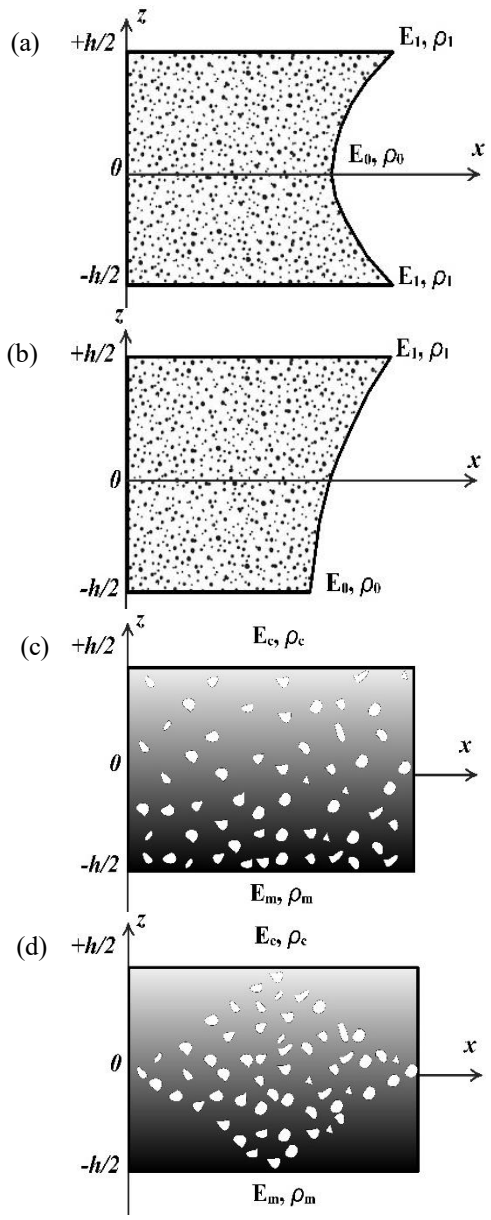

Fig. 1 Porosity distribution patterns in (FGP) beam: (a) Type-I (b) Type-II ,(c) Type- III and (d) Type-IV

2.3 Higher order shear deformation beam theory

The present theory accounts for shear deformation by a sinusoidal variation of all displacements across the thickness, and satisfies the stress-free boundary conditions on the upper and lower surfaces of the beam without requiring any shear correction factor. Moreover, the accuracy and efficiency must be improved through the obtained computations for general FGP beam problems.

2.3.1 Kinematics

Since the Euler-Bernoulli beam theory omits the effect of shear deformation and Timoshenko beam theory appropriates shear correction factors, many higher order shear deformation theories are developed and generate a host of unknowns. In this formulation, the number of unknowns and their related governing equations is reduced to three by using the following assumptions: (1) the in-plane displacements are similar to those given by the Euler-Bernoulli beam theory additionally a shear component, (2) the shear component is treated by the sinusoidal variation across the thickness coordinate in a way that transverse shear strains and stresses are given rise by this variation through the thickness of the beam, (3) the stress-free boundary conditions on the top and bottom surfaces of the beam can be affirmed without requiring any shear correction factors. Based on these assumptions, the corresponding displacement field is given and presented as follows

$$u(x,z,t) = u_0 - z\frac{\partial w_0}{\partial x} + f(z)\phi_x \tag{7a}$$

$$w(x,z,t) = w_0 \tag{7b}$$

where the axial displacement$u$, the transverse displacement w of a material point located at (x, z) in the beam. u_0, w_0 represent the displacement unknowns at the neutral axis, the unknown ϕ_x presents the rotation of the cross section of the beam. Furthermore, the function *f*(z) describes nonlinear distributions of transverse shear stress through the thickness of the beam and is chosen based on the sinusoidal function

$$f(z) = \frac{h}{\pi}\sin\left(\frac{\pi z}{h}\right) \tag{8}$$

The related nonzero strains associated with the displacement field in Eq. (7) are (Reddy 2004)

$$\varepsilon_x = \frac{\partial u_0}{\partial x} - z\frac{\partial^2 w_0}{\partial x^2} + f(z)\frac{\partial \phi_x}{\partial x} \tag{9a}$$

$$\gamma_{xz} = g(z)\phi_x \tag{9b}$$

By substituting Eq. (7) into Eq. (9) the following strain-displacement relationships are obtained for the present shear deformation beam theory

$$\varepsilon_x = \varepsilon_x^0 + zk_x + f(z)\eta_x \tag{10a}$$

$$\gamma_{xz} = g(z)\gamma_{xz}^0 \tag{10b}$$

where

$$\varepsilon_x^0 = \frac{\partial u_0}{\partial x}, k_x = -\frac{\partial^2 w_0}{\partial x^2}, \eta_x = \frac{\partial \phi_x}{\partial x}, \gamma_{xz}^0 = \phi_x \tag{11}$$

and

$$g(z) = \frac{df(z)}{dz} \tag{12}$$

2.3.2 Constitutive relations

The linear constitutive relations of a FGP beam can be written as follows:

$$\begin{Bmatrix}\sigma_x \\ \tau_{xz}\end{Bmatrix} = \begin{bmatrix}C_{11} & 0 \\ 0 & C_{44}\end{bmatrix}\begin{Bmatrix}\varepsilon_x \\ \gamma_{xz}\end{Bmatrix} \tag{13}$$

where (σ_x and τ_{xz}) and (ε_x and γ_{xz}) are the stress and strain components, respectively. The stiffness coefficients, C_{ij}, can be expressed as

$$C_{11} = E(z),\ C_{44} = G(z) = \frac{E(z)}{2(1+\nu)} \tag{14}$$

2.3.3 Governing equations

Considering the variational form of Hamilton's principle, the variational governing differential equations of equilibrium are derived to formulate the problem. This principle can be described in an extended variational form as follows

$$\delta \int_{t_1}^{t_2} [K - (U + V)]dt = 0 \tag{15}$$

where $(U + V)$ is the total potential energy of the beam; which presents the sum of the strain energy and potential energy of the applied compression load, K is the kinetic energy. The variation of strain energy of the beam is given by

$$\begin{aligned} \delta\, U &= \int_V [\sigma_x \delta\, \varepsilon_x + \tau_{xz} \delta\, \gamma_{xz}]\; dV \\ &= \int_A [N_x \delta\, \varepsilon_x^0 + M_x \delta\, k_x + S_x \delta\, \eta_x + Q_{xz} \delta\, \gamma_{xz}^0]\; \mathrm{dA} \end{aligned} \tag{16}$$

Where A is the cross-section and the stress resultants N_x, M_x, S_x and Q_{xz} are defined as

$$(N_x, M_x, S_x) = \int_{-h/2}^{h/2} (1, z, f)(\sigma_x) dz, \tag{17}$$

and

$$Q_{xz} = \int_{-h/2}^{h/2} (\tau_{xz}) g(z) dz, \tag{18}$$

Where $h/2$ and $h/2$ are the top and bottom z-coordinates of FGP beam respectively. By substituting Eqs. (10) and (13) into Eq. (17), the final expressions for the stress resultants are given as

$$\begin{aligned} N_x &= A_{11}\varepsilon_x^0 + B_{11}k_x + B_{11}^s \eta_x \\ M_x &= B_{11}\varepsilon_x^0 + D_{11}k_x + H_{11}^s \eta_x \\ S_x &= B_{11}^s \varepsilon_x^0 + H_{11}^s k_x + D_{11}^s \eta_x \end{aligned} \tag{19a}$$

$$Q_{xy} = A_{44}^s \gamma_{xz}^0 \tag{19b}$$

The constitutive components for membrane, bending, coupling and transverse shear are defined by

$$\begin{aligned} &(A_{11}, B_{11}, D_{11}, B_{11}^s, H_{11}^s, D_{11}^s) \\ &= \int_{-h/2}^{h/2} C_{11}(1, z, z^2, f, zf, f^2) dz, \end{aligned} \tag{20a}$$

$$A_{44}^s = \int_{-h/2}^{h/2} C_{44}[g(z)]^2 dz, \tag{20b}$$

The variation of the potential energy of the applied compression load can be given by

$$\delta\, V = \frac{1}{2} \int_V \left[P_{0x} \left(\frac{\delta \partial w}{\partial x} \right) \left(\frac{\partial w}{\partial x} \right) \right] dV \tag{21}$$

The variation of the kinetic energy of the mass system can be written as

$$\begin{aligned} \delta\, K &= \int_V [\dot{u} \delta\, \dot{u} + \dot{w} \delta\, \dot{w}]\, \rho(z) dV \\ &= \int_A \{ (I_1 \dot{u}_0 \delta \dot{u}_0 + I_1 \dot{w}_0 \delta \dot{w}_0) \end{aligned}$$

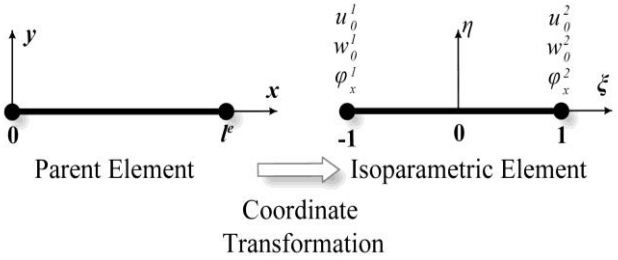

Fig. 2 Geometry and nodal degrees of freedom for two-noded isoparametric element

$$\begin{aligned} &-I_2 \left(\ddot{u}_0 \frac{\partial \delta \dot{w}_0}{\partial x} + \frac{\partial \dot{w}_0}{\partial x} \delta\, \ddot{u}_0 \right) + I_3 \left(\frac{\partial \dot{w}_0}{\partial x} \frac{\partial \delta\, \dot{w}_0}{\partial x} \right) \\ &+ I_4 (\dot{\phi} \delta\, \dot{u}_0 + \dot{u}_0 \delta\, \dot{\phi}) - I_5 \left(\dot{\phi} \frac{\partial \delta\, \dot{w}_0}{\partial x} + \frac{\partial \dot{w}_0}{\partial x} \delta\, \dot{\phi} \right) \\ &+ I_6 (\dot{\phi} \delta\, \dot{\phi}) \} dA \end{aligned} \tag{22}$$

$\rho(z)$ is the mass density; and $(I_1, I_2, I_3, I_4, I_5, I_6)$ are mass inertias defined by

$$(I_1, I_2, I_3, I_4, I_5, I_6) = \int_{-h/2}^{h/2} (1, z, z^2, f, z\, f, f^2) \rho(z) dz \tag{23}$$

Substituting Eqs. (22), (21), and (16) into Eq. (15), taking the variations of δU, δV and δK, integrating by parts, and setting each of the virtual displacements of $\delta\, u_0$, $\delta\, w_0$ and $\delta\, \phi_x$, the following weak form of governing equations of the bema are written as

$$\begin{aligned} &\int_L [\langle \delta\, \varepsilon_x^0 \rangle A_{11} \{\varepsilon_x^0\} + \langle \delta\, \varepsilon_x^0 \rangle B_{11} \{k_x\} + \langle \delta\, \varepsilon_x^0 \rangle B_{11}^s \{\eta_x\} + \\ &\langle \delta\, k_x \rangle B_{11} \{\varepsilon_x^0\} + \langle \delta k_x \rangle D_{11} \{k_x\} + \langle \delta\, k_x \rangle H_{11}^s \{\eta_x\} + \\ &\langle \delta\, \eta_x \rangle B_{11} \{\varepsilon_x^0\} + \langle \delta \eta_x \rangle D_{11} \{k_x\} + \langle \delta\, \eta_x \rangle H_{11}^s \{\eta_x\} + \\ &\langle \delta\, \gamma_{xz}^0 \rangle A_{44}^s \delta \gamma_{xz}^0 + P_0 \left\langle \frac{\delta \partial w}{\partial x} \right\rangle \left\{ \frac{\partial w}{\partial x} \right\} + \langle \delta u_0 \rangle I_1 \langle \ddot{u}_0 \rangle + \\ &\langle \delta w_0 \rangle I_1 \langle \ddot{w}_0 \rangle - \langle \delta w_0 \rangle I_2 \left\langle \frac{\partial \ddot{u}_0}{\partial x} \right\rangle - \langle \delta u_0 \rangle I_2 \left\langle \frac{\partial \ddot{w}_0}{\partial x} \right\rangle + \\ &\langle \delta w_0 \rangle I_3 \left\langle \frac{\partial^2 \ddot{w}_0}{\partial x^2} \right\rangle + \langle \delta u_0 \rangle I_4 \langle \ddot{\phi}_x \rangle + \langle \delta \phi_x \rangle I_4 \langle \ddot{u}_0 \rangle - \\ &\langle \delta w_0 \rangle I_5 \left\langle \frac{\partial \ddot{\phi}_x}{\partial x} \right\rangle - \langle \delta \phi_x \rangle I_5 \left\langle \frac{\partial \ddot{w}_0}{\partial x} \right\rangle + \langle \delta \phi_x \rangle I_6 \langle \ddot{\phi}_x \rangle] dx = 0 \end{aligned} \tag{24}$$

3. Finite element formulation

In this formulation, a two-noded finite element is developed. Consider a straight beam with length L and uniform width b and thickness h. The isoparametric transformation is often employed to derive the elementary matrices. To apply this transformation, both element geometry and displacement fields of the developed element are interpolated through the natural coordinates (Dhatt *et al.* 2012).

For the present two-noded isoparametric element, the shape functions N_i and $\bar{N}_i$ are expressed as

$$\{N_i\} = \begin{Bmatrix} N_1 \\ N_2 \end{Bmatrix} = \begin{Bmatrix} \frac{1}{2}(1 - \xi) \\ \frac{1}{2}(1 + \xi) \end{Bmatrix}$$

$$\{\bar{N}_i\} = \begin{Bmatrix} \bar{N}_1 \\ \bar{N}_2 \\ \bar{N}_3 \\ \bar{N}_4 \end{Bmatrix} = \frac{1}{4}\begin{Bmatrix} 2-3\xi+\xi^2 \\ 1-\xi-\xi^2+\xi^3 \\ 2+3\xi-\xi^2 \\ -1-\xi+\xi^2+\xi^3 \end{Bmatrix} \quad (25)$$

As previously discussed, it is clear that the above-mentioned functions guarantee the continuity requirements of displacement field: C^0 continuity for both axial displacement u_0 and rotation ϕ_x, C^1 continuity for the transverse displacement w_0 and its first derivative.

After a transformation of coordinates by using the natural coordinate system $\xi \in [-1,1]$

$$x(\xi) = \sum_{i=1}^{2} N_i(\xi) x_i = \frac{1-\xi}{2}x_1 + \frac{1+\xi}{2}x_2 \quad (26)$$

The Jacobian transformation operator relates the natural and global coordinates. The derivative with respect to the global coordinates can be determined as

$$\frac{\partial x(\xi)}{\partial \xi} = \frac{1}{L}(x_2 - x_1) = \frac{l_e}{2} = J \Rightarrow J^{-1} = \left(\frac{\partial x}{\partial \xi}\right)^{-1} = \frac{2}{l_e} \quad (27)$$

The displacement variables at any points of the element are interpolated via the shape functions as following

$$\begin{matrix} u_0(\xi) = \sum_{i=1}^{2} N_i(\xi) u_0^i \\ \phi_x(\xi) = \sum_{i=1}^{2} N_i(\xi) \phi_x^i \\ w_0(\xi) = \sum_{i=1}^{4} \bar{N}_i(\xi) w_0^i \end{matrix} \quad (28)$$

where

$$\{u_i\} = \begin{Bmatrix} u_0(\xi) \\ \phi_x(\xi) \end{Bmatrix} = \sum_1^2 \langle N_1^i(\xi) \quad N_2^i(\xi) \rangle \begin{Bmatrix} u_0^i \\ \phi_x^i \end{Bmatrix}$$

$$\{w_i\} = \begin{Bmatrix} w_0^i(\xi) \\ w_{0,x}^i(\xi) \end{Bmatrix} = \quad (29)$$

$$\sum_1^2 \langle \bar{N}_1^i(\xi) \quad \bar{N}_2^i(\xi) \quad \bar{N}_3^i(\xi) \quad \bar{N}_4^i(\xi) \rangle \begin{Bmatrix} w_0^i \\ w_{0,x}^i \end{Bmatrix}$$

Accordingly, strain-displacement relations are written as

$$\begin{matrix} \{\varepsilon_x^0\} = [B]_m \{u_0^i\} \\ \{k_x\} = [B]_f \{w_0^i\} \\ \{\eta_x\} = [B]_s \{\phi_x^i\} \\ \{\gamma_{xz}^0\} = [\bar{B}]_s \{\phi_x^i\} \end{matrix} \quad (30)$$

where $[B]$ presents the strain-displacement derivative matrix, $[B]_m$, $[B]_f$, $[\boldsymbol{B}]_s$ $[\bar{B}]_s$ and $[B]_0$ are the membrane, bending, shear, higher-order shear and geometric derivative operator matrices given by

$$\begin{matrix} [B]_m = \sum_1^2 \langle N_1 \quad 0 \quad 0 \quad 0 \quad N_2 \quad 0 \quad 0 \quad 0 \rangle_i ; \\ [B]_f = \\ \sum_1^2 \langle 0 \quad 0 \quad -\bar{N}_{1,xx} \quad -\bar{N}_{1,xx} \quad 0 \quad 0 \quad -\bar{N}_{2,xx} \quad -\bar{N}_{2,xx} \rangle_i ; \\ [B]_s = \sum_1^2 \langle 0 \quad N_{1,x} \quad 0 \quad 0 \quad 0 \quad N_{2,x} \quad 0 \quad 0 \rangle_i ; \\ [\bar{B}]_s = \sum_1^2 \langle 0 \quad N_1 \quad 0 \quad 0 \quad 0 \quad N_2 \quad 0 \quad 0 \rangle_i ; \\ [B]_0 = \sum_1^2 \langle 0 \quad 0 \quad \bar{N}_{1,x} \quad 0 \quad 0 \quad 0 \quad \bar{N}_{1,x} \quad 0 \rangle ; \end{matrix} \quad (31)$$

Introducing Eq. (31) into Eq. (24) yields the nodal contributions to the element stiffness, geometric and mass matrices and takes the form

$$\begin{matrix} \langle \delta u_i \rangle \Big[\int_{-1}^{1} (B_m^T A_{11} B_m + B_m^T B_{11} B_b + B_m^T B_{11}^s B_s \\ + B_s^T B_{11} B_m \\ + B_b^T D_{11} B_b + B_b^T H_{11}^s B_s + B_s^T B_{11} B_m + B_s^T D_{11} B_b + \\ B_s^T H_{11}^s B_s + \bar{B}_s^T A_{44}^s \bar{B}_s + P_0 B_0^T B_0 + N^T I_1 N + \bar{N}^T I_1 \bar{N} - \\ \bar{N}^T I_2 N_{,x} - N^T I_2 \bar{N}_{,x} + \bar{N}^T I_3 \bar{N}_{,xx} + N^T I_4 N + N^T I_4 N - \\ \bar{N}^T I_5 N_{,x} - N^T I_5 \bar{N}_{,x} + N^T I_6 N) J d\xi \Big] \{u_i\} = 0 \end{matrix} \quad (32)$$

Eq. (32) takes following form to conduct buckling eigenvalue analysis

$$\left([K]_g - P_0 [G]_g\right)\{u_i\} = 0 \quad (33)$$

After rewriting Eq. (32), the free vibration eigenvalue analysis is obtained in the form

$$\left([K]_g - P_0 [G]_g - \omega^2 [M]_g\right)\{u_i\} = 0 \quad (34)$$

where P_0 and ω present the critical buckling load and angular frequency respectively.

The global form of the stiffness, geometric and mass matrices are given by

$$\begin{matrix} [K]_g = \sum_e ([K]_m + [K]_{mb} + [K]_{ms} + [K]_{bm} + \\ [K]_b + [K]_{bs} + [K]_{sm} + [K]_{sb} + [K]_s + [\bar{K}]_s) \end{matrix} \quad (35a)$$

$$[G]_g = \sum_e [K]_0 \quad (35b)$$

$$\begin{matrix} [M]_g = \sum_e ([M]_m + [M]_b + [M]_{bm}^1 + [M]_{mb}^1 + \\ [M]_b^2 + [M]_{bs} + [M]_{sm} + [M]_{bs}^1 + [M]_{sb}^1 + [M]_s) \end{matrix} \quad (35c)$$

These matrices are assembled by the element stiffness matrix, the element geometric matrix and the element mass matrix. In which, they are evaluated numerically by using Gauss quadrature rule as following formulae

$$\begin{matrix} [K]_m = \int_{-1}^{1} (B_m^T A_{11} B_m) J d\xi \ ; \\ [K]_{mb} = \int_{-1}^{1} (B_m^T B_{11} B_b) J d\xi \\ [K]_{ms} = \int_{-1}^{1} (B_m^T B_{11}^s B_s) J d\xi \ ; \\ [K]_{bm} = \int_{-1}^{1} (B_s^T B_{11} B_m) J d\xi \\ [K]_b = \int_{-1}^{1} (B_b^T D_{11} B_b) J d\xi \ ; \\ [K]_{bs} = \int_{-1}^{1} (B_b^T H_{11}^s B_s) J d\xi \\ [K]_{sm} = \int_{-1}^{1} (B_s^T B_{11} B_m) J d\xi \ ; \\ [K]_{sb} = \int_{-1}^{1} (B_s^T D_{11} B_b) J d\xi \\ [K]_s = \int_{-1}^{1} (B_s^T H_{11}^s B_s) J d\xi \ ; \\ [\bar{K}]_s = \int_{-1}^{1} (\bar{B}_s^T A_{44}^s \bar{B}_s) J d\xi \end{matrix} \quad (36)$$

and

$$[G] = \int_{-1}^{1} (B_0^T B_0) J d\xi \quad (37)$$

Table 1 Material properties used in the FGP beams

Properties		Metal	Ceramic
Al-Al_2O_3	E (GPa)	70	380
	υ	0.30	0.30
	ρ (kg/m^3)	2702	3960
open-cell steel foam	E_1 (GPa)	200	/
	υ	1/3	/
	ρ_1 (kg/m^3)	7850	/

and

$$[M]_m = \int_{-1}^{1} (N^T I_1 N) J d\xi \quad ;$$

$$[M]_b = \int_{-1}^{1} (\bar{N}^T I_1 \bar{N}) J d\xi$$

$$[M]_{bm}^1 = -\int_{-1}^{1} \left(N^T I_2 \bar{N}_{,x}\right) J d\xi \quad ;$$

$$[M]_{mb}^1 = -\int_{-1}^{1} \left(\bar{N}^T I_2 N_{,x}\right) J d\xi$$

$$[M]_b^2 = \int_{-1}^{1} \left(\bar{N}^T I_3 \bar{N}_{,xx}\right) J d\xi \quad ;$$

$$[M]_{bs} = \int_{-1}^{1} (N^T I_4 N) J d\xi$$

$$[M]_{bs} = \int_{-1}^{1} \left(\bar{N}^T I_5 N_{,x}\right) J d\xi \quad ;$$

$$[M]_{sm} = -\int_{-1}^{1} \left(\bar{N}^T I_5 N_{,x}\right) J d\xi$$

$$[M]_{bs}^1 = -\int_{-1}^{1} \left(N^T I_5 \bar{N}_{,x}\right) J d\xi \quad ; [M]_s = (N^T I_6 N) J d\xi \tag{38}$$

Recall that the element stiffness, geometric, and mass matrices are exactly evaluated at sampling two points in the Gauss quadrature, except element shear stiffness is computed by using one point in Gauss quadrature to avoid shear-locking phenomenon (the reduced integration technique in Dhatt *et al.* 2012).

4. Numerical results and discussion

The free vibration and buckling analysis of FGP beams are investigated in this section; and the material properties used in the present study are illustrated in Table 1.

Dimensionless buckling loads and natural fundamental frequencies are utilized as follow:

- For porosity distribution patterns *I* and *II* (to compare with Chen *et al.* 2016)

$$\hat{\omega} = \omega L \sqrt{\frac{I_1}{A_{11}}} \quad ; \quad \hat{P}_{\text{cr}} = \frac{P_{\text{cr}}}{A_{11}}; \tag{39a}$$

- For porosity distribution patterns *III* and *IV*

Table 2 Comparison of dimensionless natural frequency $\bar{\omega}$ of perfect FG Al_2O_3 beams with various boundary conditions, material index p and length-to-thickness ratio (L/h)

BCs	L/h	Theories	p					
			0	0.5	1	2	5	10
S-S	5	TBT[(a)]	5.1525	4.4075	3.9902	3.6344	3.4312	3.3135
		Nguyan *et al.* (2015)	5.1528	4.4102	3.9904	3.6264	3.4009	3.2815
		TSBT[(b)]	5.1527	4.4107	3.9904	3.6264	3.4012	3.2816
		Present	5.1531	4.4019	3.9713	3.5971	3.3722	3.2644
	20	TBT[(a)]	5.4603	4.6514	4.2051	3.8368	3.6509	3.5416
		Nguyan *et al.* (2015)	5.4603	4.6506	4.2051	3.8361	3.6485	3.5390
		TSBT[(b)]	5.4603	4.6516	4.2050	3.8361	3.6485	3.5390
		Present	5.4603	4.6505	4.2037	3.8340	3.6463	3.5377
CC	5	TBT[(a)]	10.0705	8.7467	7.9503	7.1767	6.4935	6.1652
		Nguyan *et al.* (2015)	10.0726	8.7463	7.9518	7.1776	6.4929	6.1658
		TSBT[(b)]	10.0699	8.7463	7.9499	7.1766	6.4940	6.1652
		Present	10.0771	8.7510	7.9550	7.1794	6.4893	6.1669
	20	TBT[(a)]	12.2235	10.4263	9.4314	8.6040	8.1699	7.9128
		Nguyan *et al.* (2015)	12.2243	10.4269	9.4319	8.5977	8.1446	7.8860
		TSBT[(b)]	12.2238	10.4287	9.4316	8.5975	8.1448	7.8859
		Present	12.2225	10.4268	9.4309	8.5966	8.1423	7.8840
CF	5	TBT[(a)]	1.8948	1.6174	1.4630	1.3338	1.2645	1.2240
		Nguyan *et al.* (2015)	1.8957	1.6182	1.4636	1.3328	1.2594	1.2187
		TSBT[(b)]	1.8952	1.6182	1.4633	1.3325	1.2592	1.2183
		Present	1.8954	1.6181	1.4634	1.3326	1.2590	1.2183
	20	TBT[(a)]	1.9496	1.6604	1.5010	1.3697	1.3038	1.2650
		Nguyan *et al.* (2015)	1.9496	1.6602	1.5011	1.3696	1.3696	1.2646
		TSBT[(b)]	1.9495	1.6605	1.5011	1.3696	1.3033	1.2645
		Present	1.9496	1.6603	1.5010	1.3696	1.3033	1.2645

(a) Timoshenko beam theory by Simsek (2010).
(b) Third-order shear beam theory by Simsek (2010).

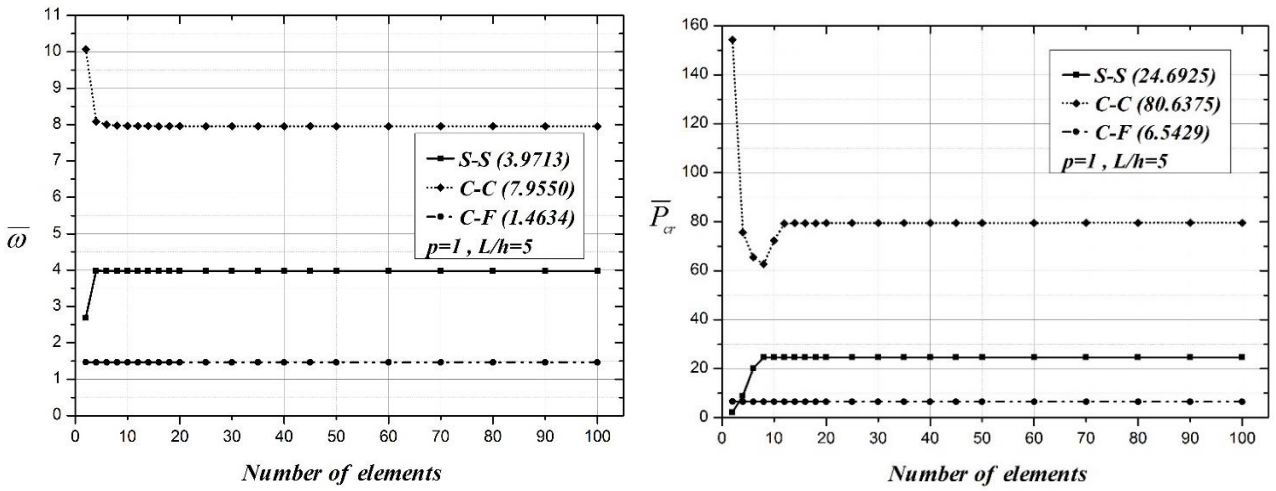

Fig. 3 Convergence of the adimensional fundamental frequency and critical buckling load of FG beams (The magnitude of convergence is represented by values in parentheses)

Table 3 Comparison of dimensionless critical buckling load $\bar{P}_{cr}$ of perfect FG Al_2O_3 beams with various boundary condi tions, material index p and length-to-thickness ratio (L/h)

BCs	L/h	Theories	p					
			0	0.5	1	2	5	10
S-S	5	TBT[(a)]	48.8350	31.9670	24.6870	19.2450	16.0240	14.4270
		Nguyan *et al.* (2015)	48.8406	32.0013	24.6894	19.1577	15.7355	14.1448
		TSBT[(b)]	48.8401	32.0094	24.6911	19.1605	15.7400	14.1468
		Present	48.8474	32.0129	24.6925	19.1571	15.7251	14.1412
	10	TBT[(a)]	52.3090	33.9960	26.1710	20.4160	17.1920	15.6120
		Nguyan *et al.* (2015)	52.3083	34.0002	26.1707	20.3909	17.1091	15.5278
		TSBT[(b)]	52.3082	34.0087	26.1727	20.3936	17.1118	15.5291
		Present	52.3100	34.0087	26.1716	20.3908	17.1060	15.5266
CC	5	TBT[(a)]	154.3500	103.2200	80.4980	62.6140	50.3840	44.2670
		Nguyan *et al.* (2015)	154.5610	103.7167	80.5940	61.7666	47.7174	41.7885
		TSBT[(b)]	154.5500	103.7490	80.6087	61.7925	47.7562	41.8042
		Present	154.5545	103.8030	80.6375	61.7707	47.6356	41.7705
	10	TBT[(a)]	195.3400	127.8700	98.7490	76. 6538	62.9580	56.5926
		Nguyan *et al.* (2015)	195.3623	128.0053	98.7885	76.6538	62.9580	56.5926
		TSBT[(b)]	195.3610	128.0500	98.7868	76.6677	62.9786	56.5971
		Present	195.3615	128.0513	98.7705	76.6291	62.9007	56.5647
CF	5	TBT[(a)]	13.2130	8.5782	6.6002	5.1495	4.3445	3.9501
		Nguyan *et al.* (2015)	13.0771	8.5000	6.5427	5.0977	4.2772	3.8820
		TSBT[(b)]	13.0771	8.5020	6.5428	5.0979	4.2776	3.8821
		Present	13.0775	8.5022	6.5429	5.0977	4.2765	3.8816
	10	TBT[(a)]	13.2130	8.5666	6.6570	5.1944	4.3903	3.9969
		Nguyan *et al.* (2015)	13.3741	8.6694	6.6678	5.2025	4.3974	4.0045
		TSBT[(b)]	13.3742	8.6714	6.6680	5.2027	4.3976	4.0046
		Present	13.3138	8.6370	6.6425	5.1812	4.3726	3.9793

(a) Timoshenko beam theory by Li and Batra (2013).
(b) Third-order shear beam theory by Vo *et al.* (2014).

$$\bar{\omega} = \omega\left(\frac{L^2}{h}\right)\sqrt{\frac{\rho_m}{E_m}} \quad ; \quad \bar{P}_{\text{cr}} = P_{\text{cr}}\frac{12L^2}{E_m h^3}; \tag{39b}$$

4.1 Evaluation and validation.

In this section, the formulated element is tested against earlier studies in the published data. For this purpose, the free vibration and buckling analyses of perfect FG beams are investigated to make a bridge to FG beams with porosity cases treated in the next sections. The first example aims to examine the convergence and validity of the formulated beam element. Fig. 3 represents the obtained adimensional fundamental frequencies and critical buckling loads of FG beams with different boundary conditions and the number

Table 4 Comparison of dimensionless natural frequency $\hat{\omega}$ of imperfect FG beams with various boundary conditions and length-to-thickness ratio (L/h) with e_0=0.50

BCs	L/h	Porosity distribution I			Porosity distribution II		
		Chen *et al.* (2016)	ANSYS	Present	Chen *et al.* (2016)	ANSYS	Present
S-S	10	0.2798	0.2778	0.2791	0.2599	0.2549	0.2548
	20	0.1422	0.1419	0.1421	0.1318	0.1296	0.1292
	50	0.0571	0.0571	0.0571	0.0529	0.0521	0.0519
C-C	10	0.5944	0.6101	0.5897	0.5475	0.5600	0.5476
	20	0.3166	0.3176	0.3158	0.2888	0.2941	0.2887
	50	0.1291	0.1289	0.1291	0.1174	0.1183	0.1174
C-F	10	0.1008	0.1007	0.1007	0.0917	0.0920	0.0917
	20	0.0508	0.0508	0.0508	0.0462	0.0463	0.0462
	50	0.0204	0.0204	0.0204	0.0185	0.0186	0.0185

Table 5 Comparison of first six dimensionless natural frequencies $\hat{\omega}$ of imperfect FG Clamped-Free beams with v arious length-to-thickness ratio (L/h) and porosity coefficients (e_0)

Porosity model	L/h	e_0	Theories	*Mode*					
				1	2	3	4	5	6
Porosity distribution I	10	0.20	Chen *et al.* (2016)	0.1003	0.5966	1.5193	1.5549	2.7936	4.2217
			Present	0.1003	0.5962	1.5193	1.5536	2.7920	4.2164
		0.50	Chen *et al.* (2016)	0.1008	0.5963	1.4379	1.5439	2.7555	4.1400
			Present	0.1007	0.5929	1.4379	1.5278	2.7151	4.0614
		0.80	Chen *et al.* (2016)	0.1050	0.6149	1.3668	1.5746	2.7800	4.1005
			Present	0.1046	0.6012	1.3668	1.5110	2.6232	3.8506
	20	0.20	Chen *et al.* (2016)	0.0505	0.3121	0.8555	1.5193	1.6282	2.6066
			Present	0.0505	0.3120	0.8549	1.5193	1.6264	2.5950
		0.50	Chen *et al.* (2016)	0.0508	0.3134	0.8572	1.4379	1.6266	2.5950
			Present	0.0508	0.3129	0.8539	1.4379	1.6159	2.5634
		0.80	Chen *et al.* (2016)	0.0530	0.3260	0.8879	1.3668	1.6761	2.6583
			Present	0.0529	0.3238	0.8748	1.3668	1.6351	2.5600
	50	0.20	Chen *et al.* (2016)	0.0202	0.1265	0.3530	0.6882	1.1360	1.5193
			Present	0.0202	0.1265	0.3530	0.6880	1.1296	1.5193
		0.50	Chen *et al.* (2016)	0.0204	0.1273	0.3550	0.6916	1.1406	1.4379
			Present	0.0204	0.1272	0.3547	0.6906	1.1324	1.4379
		0.80	Chen *et al.* (2016)	0.0212	0.1327	0.3699	0.7200	1.1857	1.3668
			Present	0.0212	0.1326	0.3689	0.7164	1.1708	1.3668
Porosity distribution II	10	0.20	Chen *et al.* (2016)	0.0977	0.5825	1.5187	1.5229	2.7424	4.1544
			Present	0.0977	0.5828	1.5189	1.5252	2.7512	4.1693
		0.50	Chen *et al.* (2016)	0.0917	0.5471	1.4283	1.4403	2.5791	3.9080
			Present	0.0917	0.5471	1.4288	1.4404	2.5825	3.9126
		0.80	Chen *et al.* (2016)	0.0808	0.4841	1.2730	1.3680	2.3122	3.5232
			Present	0.0807	0.4838	1.2715	1.3679	2.3093	3.5151
	20	0.20	Chen *et al.* (2016)	0.0492	0.3041	0.8344	1.5193	1.5900	2.5491
			Present	0.0492	0.3041	0.8346	1.5193	1.5905	2.5428
		0.50	Chen *et al.* (2016)	0.0462	0.2856	0.7836	1.4377	1.4938	2.3953
			Present	0.0462	0.2855	0.7835	1.4377	1.4933	2.3870
		0.80	Chen *et al.* (2016)	0.0406	0.2516	0.6919	1.3213	1.3681	2.1277
			Present	0.0406	0.2515	0.6914	1.3198	1.3680	2.1174
	50	0.20	Chen *et al.* (2016)	0.0197	0.1232	0.3439	0.6705	1.1072	1.5193
			Present	0.0197	0.1232	0.3439	0.6705	1.1014	1.5193
		0.50	Chen *et al.* (2016)	0.0185	0.1157	0.3229	0.6296	1.0396	1.4379
			Present	0.0185	0.1157	0.3228	0.6295	1.0340	1.4379
		0.80	Chen *et al.* (2016)	0.0163	0.1018	0.2842	0.5544	0.9163	1.3656
			Present	0.0163	0.1018	0.2841	0.5543	0.9110	1.3510

of elements for the span-to-height ratio (L/h=5) and the power-law index (p=1). For the given problem, the formulated finite element model has a perfect convergence rate. Furthermore, as the mesh is refined and the number of degrees of freedom increases, the solution error decreases at a constant rate. The convergence diagram depicts a straight

Table 6 Comparison of first five dimensionless natural frequencies $\bar{\omega}$ of imperfect FG Clamped-Clamped beams with various length-to-thickness ratio (L/h) with e_0=0.50

Porosity model	L/h	Theories	Mode				
			1	2	3	4	5
Porosity distribution I	5	EBT[(a)]	6.3393	14.3794	16.5216	28.7624	30.0004
		Wu *et al.* (2018)	5.0185	11.2724	14.3794	18.6110	26.4276
		Noori *et al.* (2021)	5.0184	11.2715	14.3789	18.6071	26.4166
		Present	4.9467	11.1247	14.3794	18.4461	26.2926
	20	EBT[(a)]	6.4716	17.7708	34.6311	56.7868	57.5187
		Wu *et al.* (2018)	6.3476	17.0542	32.3755	51.5447	57.5178
		Noori *et al.* (2021)	6.3476	17.0537	32.3734	51.5379	57.5154
		Present	6.3326	16.9736	32.1384	51.0291	57.5178
	50	EBT[(a)]	6.4792	17.8492	34.9578	57.7105	86.0649
		Wu *et al.* (2018)	6.4588	17.7265	34.5502	56.6999	83.9717
		Noori *et al.* (2021)	6.4588	17.7262	34.5490	56.6964	83.9634
		Present	6.4561	17.7102	34.4967	56.5683	83.7011
Porosity distribution II	5	EBT[(a)]	5.7687	14.3658	15.1039	27.4569	28.8300
		Wu *et al.* (2018)	4.7216	10.7878	14.3780	17.9640	25.6576
		Noori *et al.* (2021)	4.7215	10.7869	14.3732	17.9603	25.6471
		Present	4.7445	10.9278	14.3734	18.3320	26.3433
	20	EBT[(a)]	5.8807	16.1529	31.4917	51.6680	57.5170
		Wu *et al.* (2018)	5.7872	15.6088	29.7656	47.6214	57.5161
		Noori *et al.* (2021)	5.7872	15.6083	29.7636	47.6149	57.5138
		Present	5.7864	15.6060	29.7604	47.6151	57.5160
	50	EBT[(a)]	5.8872	16.2191	31.7679	52.4504	78.2314
		Wu *et al.* (2018)	5.8718	16.1267	31.4604	51.6863	76.6454
		Noori *et al.* (2021)	5.8718	16.1263	31.4590	51.6826	76.6366
		Present	5.8716	16.1253	31.4559	51.6750	76.6209

(a) Euler-Bernoulli beam theory by Wu *et al.* (2018).

Table 7 Comparison of dimensionless natural frequency $\bar{\omega}$ of imperfect Clamped-Clamped FG AI_2O_3 beams with various length-to-thickness ratio (L/h), material index p and porosity coefficients e_0

Type of porosity	e_0	Theories	p	L/h				
				5	10	15	20	50
/	0	Fazzolari (2018)	0.20	9.510418	10.902077	11.230206	11.349936	11.478317
		Present		9.470002	10.893399	11.248740	11.383257	11.535506
		Fazzolari (2018)	1	8.058737	9.157737	9.412606	9.504972	9.603410
		Present		7.955046	9.057966	9.328770	9.430800	9.5459588
		Fazzolari (2018)	5	6.550907	7.730205	8.011787	8.115440	8.230252
		Present		6.489312	7.695104	8.017731	8.142493	8.285674
Porosity distribution III	0.20	Fazzolari (2018)	0.20	9.699950	11.065078	11.387708	11.506416	11.636060
		Present		9.663921	11.102034	11.460112	11.595557	11.748783
		Fazzolari (2018)	1	7.738870	8.680612	8.896207	8.974618	9.059443
		Present		7.634211	8.607706	8.842584	8.930633	9.029711
		Fazzolari (2018)	5	5.274587	6.169857	6.401280	6.489091	6.587350
		Present		5.238701	6.127511	6.361369	6.451452	6.554576
Porosity distribution VI	0.20	Fazzolari (2018)	0.20	9.722932	11.175035	11.521018	11.647945	11.785007
		Present		9.649402	11.162933	11.545350	11.69065	11.855480
		Fazzolari (2018)	1	8.098449	9.232496	9.499400	9.596846	9.701639
		Present		7.974245	9.129961	9.417318	9.526001	9.648962
		Fazzolari (2018)	5	6.113225	7.380488	7.667772	7.773786	7.891232
		Present		6.091594	7.413306	7.787405	7.934963	8.106414

line after using a few numbers of elements, which indicates that the solution error decreases proportionally to the mesh size.

Next, the fundamental natural frequencies and critical buckling loads obtained by the present element are studied and compared with other FG beam theories. In Table 2, the fundamental frequencies of FG beam are presented with various values of material index p and length-to-thickness ratio (L/h) and supported by many general boundary conditions. The present computed dimensionless fundamental frequencies are compared to those of other shear beam theories such as the Timoshenko beam theory of

Table 8 Comparisons of dimensionless natural frequency $\bar{\omega}$ of imperfect Clamped-Free FG AI_2O_3 beams with various length-to-thickness ratio (*L/h*), material index *p* and porosity coefficients e_0

Type of porosity	e_0	Theories	*p*	*L/h*				
				5	10	15	20	50
	0	Fazzolari (2018)	0.20	1.764354	1.795134	1.800197	1.801716	1.802894
		Present		1.766027	1.804055	1.811487	1.814122	1.816990
		Fazzolari (2018)	1	1.477720	1.502145	1.506082	1.507242	1.508116
		Present		1.463376	1.493174	1.498986	1.501046	1.503288
		Fazzolari (2018)	5	1.260205	1.286396	1.290818	1.292230	1.293647
		Present		1.258958	1.293921	1.300856	1.303324	1.306016
Porosity distribution III	0.20	Fazzolari (2018)	0.20	1.788152	1.820249	1.825900	1.827737	1.829459
		Present		1.799126	1.837484	1.844977	1.847633	1.850524
		Fazzolari (2018)	1	1.395065	1.417595	1.421474	1.422714	1.423856
		Present		1.386211	1.412687	1.417838	1.419662	1.421647
		Fazzolari (2018)	5	1.003448	1.028710	1.033336	1.034873	1.036384
		Present		0.996532	1.023469	1.028815	1.0307183	1.032794
Porosity distribution VI	0.20	Fazzolari (2018)	0.20	1.809381	1.842829	1.848496	1.850252	1.851722
		Present		1.812583	1.853621	1.861662	1.864514	1.867620
		Fazzolari (2018)	1	1.490613	1.517196	1.521649	1.523015	1.524150
		Present		1.477017	1.508818	1.515039	1.517245	1.519646
		Fazzolari (2018)	5	1.205732	1.100163	1.237786	1.239359	1.240955
		Present		1.223388	1.264299	1.272518	1.275452	1.278658

Simsek (2010), higher-order shear deformation beam theory used by Nguyan *et al.* (2015), and the third-order shear deformation beam theory of Vo *et al.* (2014). A similar investigation is performed for the buckling analysis of FG beams.

The computed dimensionless critical buckling loads are presented in Table 3. It is seen that the obtained results present a closer agreement with those given by using other shear beam theories for both free vibration and buckling analysis. As should be noted, the Timoshenko beam theory needs an appropriate shear correction factor to exactly evaluate the shear stress; this factor is dependent on various parameters such as geometry, material properties, and imposed boundary conditions. Thus, more supplementary operations are required. The computations given by Nguyan *et al.* (2015) are founded on higher-order shear deformation beam theory via analytical solutions, the sensitivity of given solutions is concerned with the number of terms relative to opted admissible functions and used boundary conditions that are complicated in computer implantation. The results given by Vo *et al.* (2014) are derived using the classical finite element method, which is cumbersome and computationally expensive. In this spirit, the formulated element is typically faster to simulate than its finite element counterparts by including the isoparametric concept, and the obtained results achieve the same efficiency and precision.

4.2 Free vibration analysis of imperfect FG beams

In this subsection, various numerical studies on the free vibration analysis of imperfect FG beams are presented with many distributions of porosities. Table 4 presents a comparative study of the obtained results with those reported by Chen *et al.* (2016). A closer inspection of Table 4 confirms the validity and precision of the obtained results. Moreover, it should be noted that the results given by Chen *et al.* (2016) are derived using Ritz solutions of the Timoshenko beam theory, which include the shear correction factor, and the ANSYS results are obtained using the four-node element SHELL181. The effect of porosity patterns has a significant impact on computed dimensionless frequencies; a high difference arises in an important length-to-thickness ratio (*L/h*) and decreases in thin beam cases, this observation emerges in the clamped-clamped boundary condition. As expected, the porosity pattern could be attributed to reducing the resulting stiffness and mass matrices and the porosity distribution type-II is more concerning.

In Table 5, the influence of the length-to-thickness ratio (*L/h*) and porosity parameter on the first six dimensionless natural frequencies is investigated for imperfect FG beams, this example presents an additional test to ensure the accuracy of obtained results, it is clear that the effect of length-to-thickness ratio is more remarkable than porosity parameter and the dimensionless fundamental frequencies increase as the increase of the porosity parameter, the length-to-thickness ratio (*L/h*) contributes to reducing slightly the difference of dimensionless frequencies from thick to thin imperfect FG beams, this observation is validated for the obtained first six dimensionless natural frequencies.

Next, the comparison of the first five dimensionless natural frequencies of clamped-clamped imperfect beams versus other theories is illustrated in Table 6. Again, the obtained results agree closely with those obtained by applying the Timoshenko and Euler-Bernoulli beam theories. It should be noted that those beam theories slightly overpredict the frequencies of thick beams; this may be explained by the presence of the shear deformation effect. On other hand, this effect must be treated with more detailed information, such as the appropriate shear correction factor and the shear-locking phenomenon. The

Table 9 Comparisons of dimensionless critical buckling load $\bar{P}_{cr}$ of imperfect Clamped-Clamped FG AI_2O_3 beams with various length-to-thickness ratio (L/h), material index p and porosity coefficients e_0

Type of porosity	e_0	Theories	p	L/h				
				5	10	15	20	50
	0	Fazzolari (2018)	0.50	10.393947	11.240275	11.470924	11.513742	11.528689
		Present		10.623640	11.322995	11.512715	11.548559	11.561159
		Fazzolari (2018)	1	8.060210	8.711658	8.889274	8.922276	8.933803
		Present		8.195891	8.714282	8.854492	8.880962	8.890265
		Fazzolari (2018)	5	5.053081	5.567317	5.711452	5.739002	5.748738
		Present		5.209947	5.692777	5.828080	5.853858	5.862935
Porosity distribution III	0.1	Fazzolari (2018)	0.50	9.367377	10.116714	10.321983	10.360305	10.373706
		Present		9.597628	10.217570	10.385511	10.417211	10.428359
		Fazzolari (2018)	1	6.943418	7.488209	7.637307	7.665153	7.674896
		Present		7.075855	7.503988	7.619406	7.641177	7.648828
		Fazzolari (2018)	5	3.881263	4.321306	4.448823	4.473115	4.481662
		Present		3.962531	4.323427	4.424388	4.443615	4.450141
	0.2	Fazzolari (2018)	0.50	8.330615	8.983116	9.162496	9.196134	9.207915
		Present		8.558145	9.097673	9.097673	9.271083	9.280759
		Fazzolari (2018)	1	5.787381	6.223798	6.343400	6.365822	6.373678
		Present		5.913237	6.248399	6.338340	6.355286	6.361238
		Fazzolari (2018)	5	2.468453	2.743841	2.824293	2.839707	2.845140
		Present		2.547066	2.755594	2.813318	2.824280	2.828137
Porosity distribution VI	0.1	Fazzolari (2018)	0.50	10.103839	10.937603	11.165691	11.208124	11.222944
		Present		10.324135	11.021781	11.211439	11.247291	11.259894
		Fazzolari (2018)	1	7.725177	8.360591	8.534645	8.567062	8.578391
		Present		7.854629	8.364556	8.502759	8.528864	8.538039
		Fazzolari (2018)	5	4.571055	5.048363	5.182247	5.207807	5.216830
		Present		4.778540	5.264372	5.401985	5.428277	5.437540
	0.2	Fazzolari (2018)	0.50	9.810828	10.632613	10.858304	10.900382	10.915087
		Present		10.020446	10.717010	10.906819	10.942721	10.955344
		Fazzolari (2018)	1	7.381259	8.000770	8.171313	8.203155	8.214290
		Present		7.503984	8.005131	8.141264	8.166993	8.176038
		Fazzolari (2018)	5	4.083984	4.528771	4.653653	4.677474	4.685878
		Present		4.305361	4.797350	4.938805	4.965937	4.975505

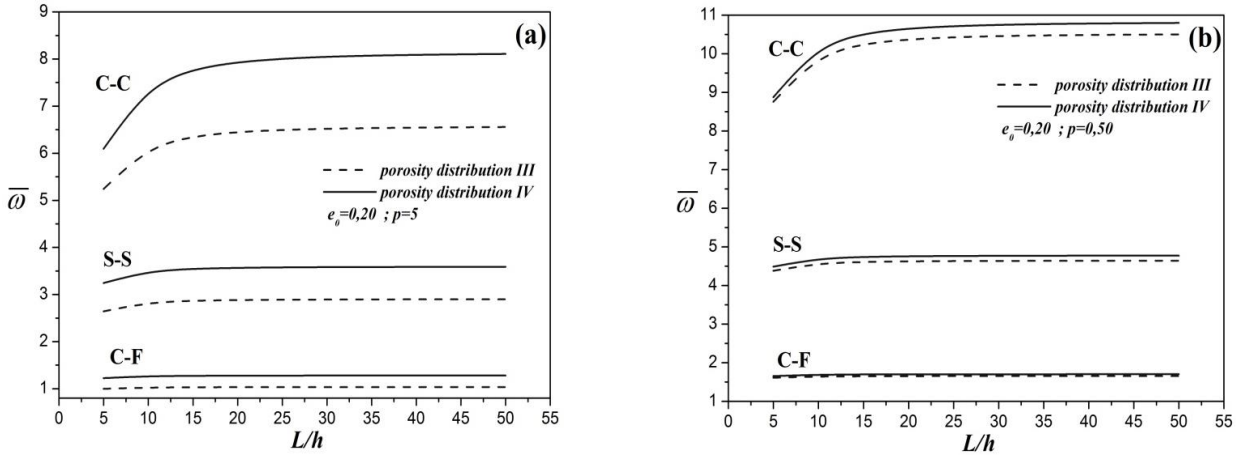

Fig. 4 Variation of dimensionless fundamental frequency $\bar{\omega}$ versus the length-to-thickness ratio (L/h) with various boundary conditions: (a) FGP Al_2O_3 beams (e_0=0.20 and p=5), (b) FGP Al_2O_3 beams (e_0=0.20 and p=0.50)

developed element demonstrates that the same effect can be efficiently viewed using an advanced finite element formulation that is free of numerical problems.

To further verify the effect of porosity on free vibration analysis of FGP beams, two other porosity distribution models are considered. Dimensionless natural frequencies are computed and compared to those given by Fazzolari (2018) for various length-to-thickness ratios (L/h), material index p, and porosity coefficients (e_0). The obtained results are presented for clamped-clamped and clamped-free boundary conditions in Tables 7 and 8, respectively.

The obtained dimensionless natural frequencies are in

Table 10 Benchmark results for first three dimensionless natural frequencies $\bar{\omega}$ of imperfect FG AI_2O_3 beams with various boundary conditions, material index p and porosity coefficients e_0.(L/h=5)

BCs	e_0	p	Porosity III			Porosity VI		
			1	2	3	1	2	3
CC	0.20	0.5	8.7558	20.4822	27.6714	8.8736	20.5906	27.4421
		1	7.6341	17.9668	25.2530	7.9742	18.5358	25.2746
		5	5.2385	11.9203	17.5024	6.0915	13.5450	18.8242
	0.30	0.5	8.7461	20.5065	27.9558	8.9395	20.6847	27.5491
		1	7.3333	17.3732	25.2123	7.9765	18.4859	25.2589
		5	3.2178	7.6908	13.1476	5.7616	12.6524	18.1348
	0.40	0.5	8.7176	20.5049	28.3209	9.0087	20.7799	27.6677
		1	6.8088	16.3099	25.1428	7.9716	18.4139	25.2387
		5	3.4186	6.9485	10.3563	5.2557	11.3522	17.1426
S-S	0.20	0.5	4.3802	13.4501	15.7363	4.4872	13.4455	15.8848
		1	3.7579	11.6599	14.1080	3.9977	12.0089	14.5011
		5	2.6403	7.5808	9.9979	3.2421	8.8424	11.2582
	0.30	0.5	4.3576	13.4774	15.7892	4.5344	13.4837	16.0130
		1	3.5660	11.2195	13.8393	4.0085	11.9531	14.5328
		5	1.4574	4.4137	6.9252	3.1279	8.4313	10.7454
	0.40	0.5	4.3196	13.4835	15.8503	4.5850	13.5258	16.1485
		1	3.2473	10.4093	13.3923	4.0166	11.8866	14.5560
		5	3.9229	4.3029	6.4586	2.9492	7.8721	9.9349
C-F	0.20	0.5	1.6103	8.8279	13.8674	1.6525	8.9743	13.7486
		1	1.3862	7.6337	12.7159	1.4770	8.0247	12.7114
		5	0.9965	5.2412	9.0697	1.2234	6.2417	9.6172
	0.30	0.5	1.6021	8.8039	14.0163	1.6717	9.0457	13.8051
		1	1.3166	7.2937	12.7211	1.4834	8.0275	12.7143
		5	0.5559	3.0579	7.3406	1.1904	5.9362	9.3561
	0.40	0.5	1.5883	8.7563	14.2075	1.6924	9.1209	13.8679
		1	1.2006	6.7150	12.7219	1.4891	8.0227	12.7174
		5	0.8271	2.9610	5.6679	1.1372	5.4712	9.0168

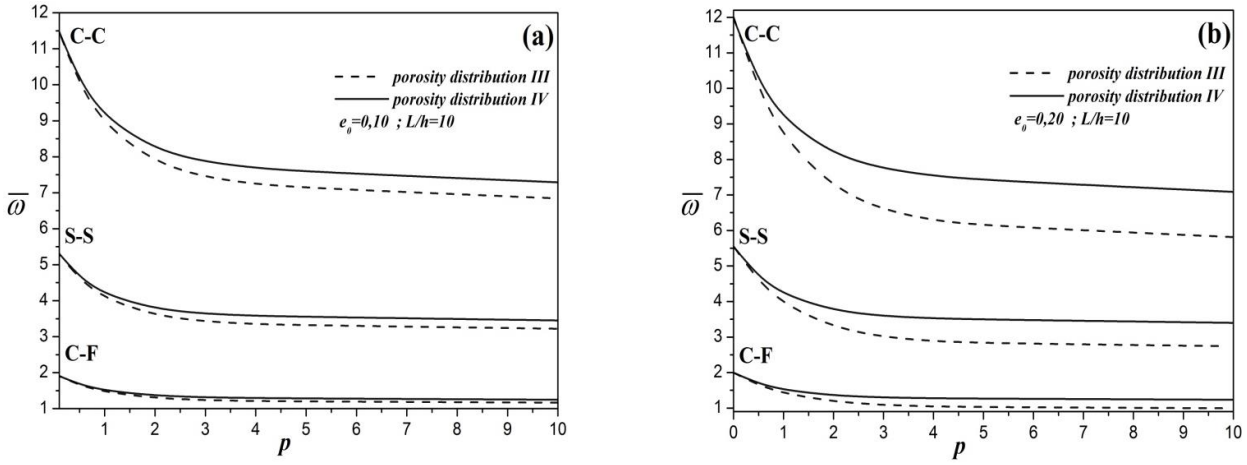

Fig. 5 Variation of dimensionless fundamental frequency $\bar{\omega}$ versus the material index (k) with various boundary conditions (a)FGP Al_2O_3 beams (e_0=0.10 and L/h=10), (b) FGP Al_2O_3 beams (e_0=0.20 and L/h=10)

good agreement with compared computations except for a slight difference marked in very thick clamped-clamped beam cases. Moreover, it should be noted that the dimensionless natural frequencies explored by Fazzolari (2018) are derived by using refined hierarchical kinematic quasi-3D beam theories and Ritz solutions, which generate even greater numbers of unknowns. In contrast to the used porosity distributions mentioned above, the porosity distribution type III and IV contribute to an increase in the dimensionless frequencies as the FG beam enters a ceramic-rich phase and decreases when the FG beam tends to transform a fully metallic state for the same porosity parameter. It is indicated that the porosity parameter produces a high magnitude of dimensionless frequencies compared to those of perfect beams; this inconsistency may be due to material property reduction in imperfect FG beams.

The effects of the thickness ratio (L/h) on the

Table 11 Benchmark results for first three dimensionless natural frequencies $\bar{\omega}$ of imperfect FG beams with various boundary conditions and porosity coefficients e_0 (L/h=5)

BCs	e_0	Porosity I			Porosity II		
		1	2	3	1	2	3
C-C	0.20	5.0523	11.6373	15.1934	5.1167	11.7081	15.1940
	0.40	4.8587	11.1862	14.6507	5.0075	11.3382	14.6539
	0.60	4.6131	10.6388	14.0994	4.8798	10.8842	14.1099
	0.80	4.2613	9.9156	13.6402	4.7176	10.2833	13.6688
S-S	0.20	2.5949	7.5883	8.9825	2.6539	7.5968	9.1105
	0.40	2.4949	7.2824	8.6604	2.6398	7.3267	8.9469
	0.60	2.3576	6.9118	8.2773	2.6386	7.0547	8.7653
	0.80	2.1392	6.4007	7.8080	2.6687	6.8342	8.5498
C-F	0.20	0.9555	5.1482	7.5970	0.9791	5.2314	7.5968
	0.40	0.9194	4.9502	7.3281	0.9775	5.1484	7.3267
	0.60	0.8700	4.6918	7.0586	0.9828	5.0612	7.0547
	0.80	0.7912	4.3078	6.8422	1.0055	4.9690	6.8342

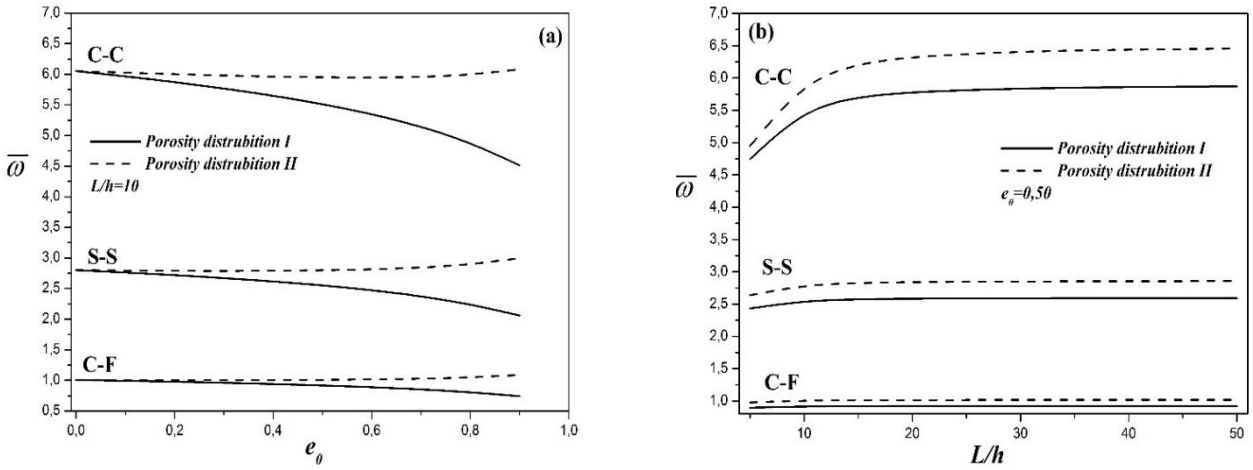

Fig. 6 Variation of dimensionless fundamental frequency $\bar{\omega}$ FGP beams with various boundary conditions (a) versus porosity coefficient (e_0) and L/h=10, (b) versus length-to-thickness ratio (L/h) and e_0=0.50

dimensionless natural fundamental frequencies $\bar{\omega}$ of FGP Al_2O_3 beams with various boundary conditions have been depicted in Fig. 4. Fig. 5 illustrates the curves of the variation of dimensionless natural fundamental frequencies $\bar{\omega}$ versus the material index p of FGP Al_2O_3 with various boundary conditions. As shown in Fig. 4. The dimensionless fundamental frequencies increase when the thickness ratio (L/h) has increased too. The effect of the material composition is also a significant parameter; the ceramic material is considered stiffer than metallic material, and therefore the dimensionless frequencies provide a higher magnitude in FGP beams as the amount of ceramic increases.

For the same porosity coefficient and boundary condition, it is also marked that the margin of difference between obtained dimensionless frequencies for both used porosity distributions slightly increases with the increasing value of thickness ratio in FGP beams as the amount of ceramic increases and this margin has grown up when FGP beams are metallic-rich phase. It has been conclusively shown that the porosity provides greater impact when the beam tends to become more metallic. For additional evidence, this observation is clearly displayed in Fig. 5.

The effect of the porosity parameter and thickness ratio is shown in Fig. 6. for both porosity distributions (Type I and Type II). The thickness ratio (L/h) contributes to an increase in dimensionless frequencies from thick to thin FGP beams, as observed. The porosity parameter is a non-trivial factor; this parameter shows the significant decreases in dimensionless frequencies of porosity distribution Type-I as the porosity parameter increases and this outcome is contrary to that of porosity distribution Type II. It seems possible that this inconsistency is due to the material property reduction in resulting stiffness and mass matrices, which involves a marked depletion in the FGP beam inertia compared to the FGP beam stiffness.

4.3 Buckling analysis of imperfect FG beams.

Continuously, the dimensionless critical buckling loads of imperfect Aluminum-Alumina FG beams with porosity distributions Type-III and Type-IV are examined and compared to those obtained by Fazzolari (2018) for various length-to-thickness ratios, material index p, and porosity coefficients. The numerical results are presented in Table 9. The obtained results are in good agreement with those given

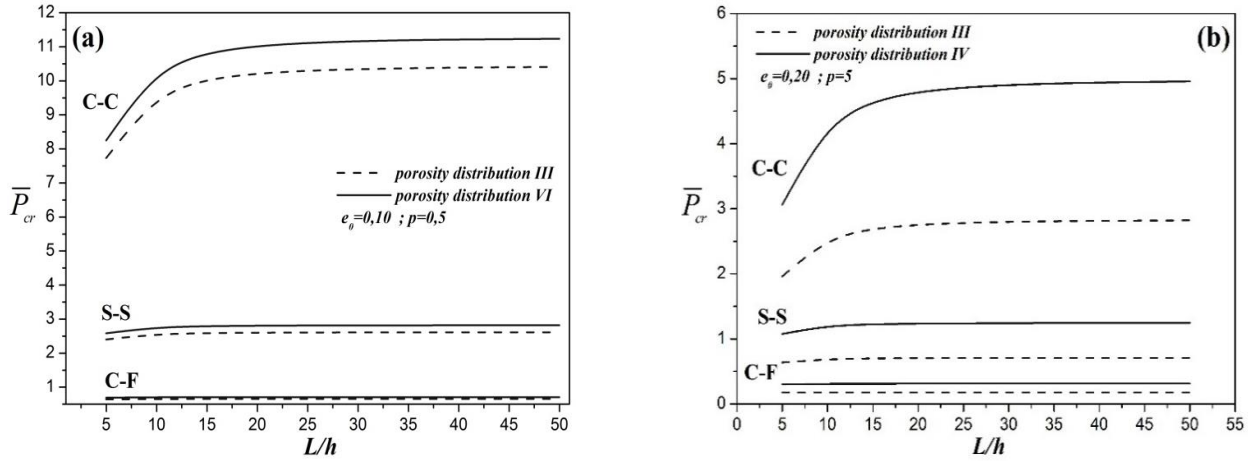

Fig. 7 Variation of dimensionless critical buckling loads $\bar{P}_{cr}$ versus the length-to-thickness ratio (L/h) with various boundary conditions: (a) FGP Al_2O_3 beams (e_0=0.10 and p=0.50), (b) FGP Al_2O_3 beams (e_0=0.20 and p=5)

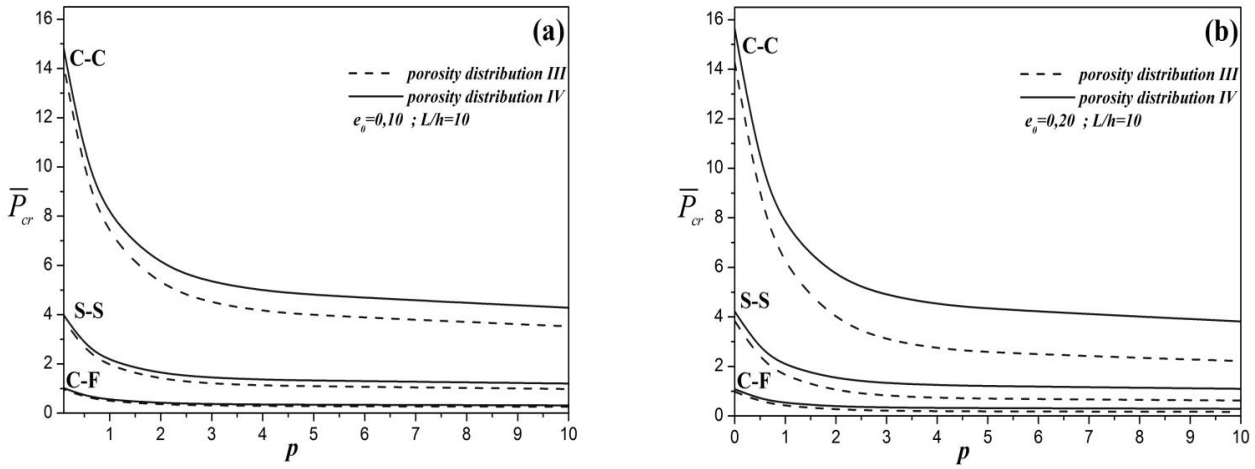

Fig. 8 Variation of dimensionless critical buckling loads $\bar{P}_{cr}$ versus the material index (k) with various boundary conditions (a) FGP Al_2O_3 beams (e_0=0.10 and L/h=10), (b) FGP Al_2O_3 beams (e_0=0.20 and L/h=10)

by Fazzolari (2018). As previously stated, the compared results are based on refined hierarchical kinematics quasi-3D beam theories using the Ritz approximation, which, unlike the finite element method, has a limit on the number of admissible function terms to avoid numerical instability. The number of generated unknowns turns the Ritz method unstable due to round-off errors.

Again, this example demonstrates the efficiency and accuracy of the developed element in buckling analysis of imperfect FG beams. As observed, the metallic-rich FG beams are more susceptible to buckling than ceramic-rich FG beams, and the porosity coefficient contributes to decreasing the critical buckling loads. Fig. 7. illustrates the effect of length-to-thickness ratio on dimensionless critical buckling loads with various boundary conditions. It is clear that the porosity contributes to reduction in the resulting stiffness matrix, and this leads to decrease the dimensionless critical buckling loads for all used boundary conditions. The difference between obtained buckling loads by using both porosity distributions is more significant with important value of porosity parameter, and this difference increases when the FGP beams becomes thinner. It is evidence that the boundary conditions play a crucial role in predicting critical buckling loads, the higher values of dimensionless critical buckling loads are observed in clamped-clamped FGP beams and the lower magnitudes for clamped-free FGP beams. As expected, the metallic-rich FG beams are more susceptible to buckling than ceramic-rich FG beams, and this is clearly presented in Fig. 8. To highlight the role of porosity and thickness ratio, the dimensionless buckling loads are presented for imperfect FG beams with various boundary conditions in Fig. 9.

A closer inspection of the figure shows that the thickness ratio inhibits the margin between dimensionless critical buckling loads obtained by using porosity distributions, and dimensionless critical buckling loads decrease when the porosity parameter increases.

4.4 Parametric study

In order to assess the effect of porosity on the free vibration and buckling analysis of imperfect FG beams, various porosity distributions are considered. Tables 10-11 present benchmark results for the first three dimensionless natural frequencies of imperfect FG beams with various boundary conditions, and material distributions through the

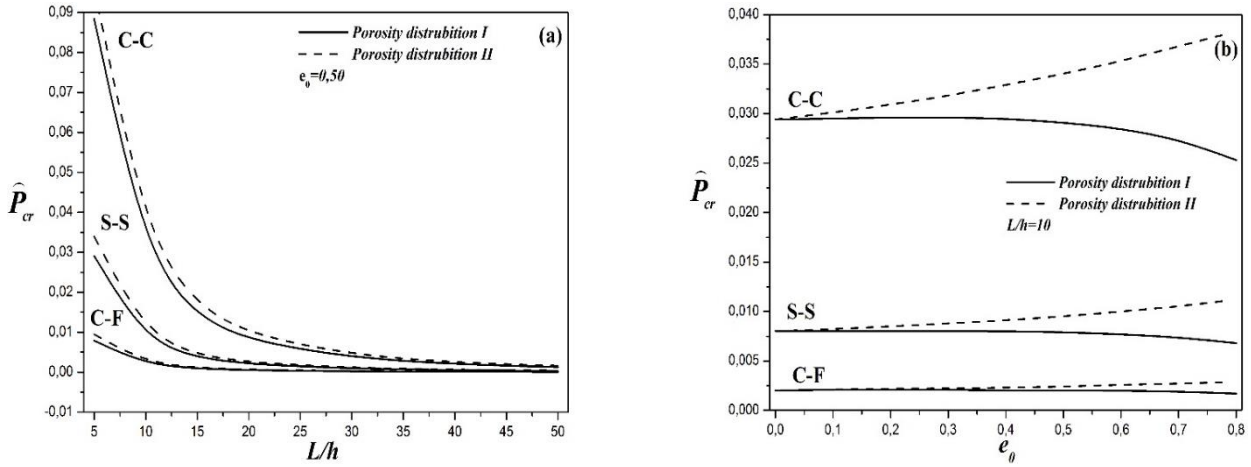

Fig. 9 Variation of dimensionless critical buckling loads $\hat{P}_{cr}$ FGP beams with various boundary conditions (a) versus length-to-thickness ratio (L/h) and e_0=0.50, (b) versus porosity coefficient (e_0) and L/h=10

Table 12 Benchmark results for first three dimensionless critical buckling loads $\bar{P}_{cr}$ of imperfect FG AI_2O_3beams with various boundary conditions, material index p and porosity coefficients e_0 (L/h=5)

BCs	e_0	p	Porosity III			Porosity IV		
			1	2	3	1	2	3
CC	0.20	0.5	6.9239	10.8028	15.8334	7.9624	12.2115	17.6562
		1	4.8734	7.7499	11.5440	6.0087	9.2869	13.5154
		5	1.9597	2.9257	4.1510	3.0622	4.2883	5.8054
	0.30	0.5	6.1036	9.5793	14.1106	7.6716	11.7009	16.8453
		1	3.9284	6.3586	9.6180	5.6862	8.7413	12.6678
		5	0.6292	1.0963	1.7791	2.5733	3.5023	4.6529
	0.40	0.5	5.2636	8.3249	12.3400	7.3747	11.1800	16.0201
		1	2.8955	4.8267	7.4948	5.3533	8.1808	11.8013
		5	0.6318	0.6488	0.6655	2.0032	2.6179	3.3911
S-S	0.20	0.5	2.1395	6.9242	11.8495	2.5051	7.9624	13.3862
		1	1.4783	4.8735	8.5029	1.8759	6.0087	10.1812
		5	0.6367	1.9597	3.2034	1.0763	3.0622	4.6837
	0.30	0.5	1.8752	6.1036	10.5066	2.4280	7.6716	12.8245
		1	1.1719	3.9284	6.9775	1.7855	5.6862	9.5815
		5	0.1763	0.6292	1.2039	0.9429	2.5733	3.8187
	0.40	0.5	1.6046	5.2637	9.1338	2.3495	7.3747	12.2514
		1	0.8410	2.8954	5.2991	1.6919	5.3533	8.9655
		5	0.6107	0.6320	0.6493	0.7853	2.0032	2.8453
C-F	0.20	0.5	0.5686	4.3821	9.4723	0.6698	5.0872	10.7912
		1	0.3905	3.0540	6.7337	0.5003	3.8234	8.1766
		5	0.1722	1.2730	2.6157	0.2998	2.0699	3.9427
	0.30	0.5	0.4974	3.8510	8.3752	0.6505	4.9167	10.3661
		1	0.3079	2.4398	5.4779	0.4771	3.6291	7.7152
		5	0.0455	0.3776	0.9105	0.2672	1.7751	3.2573
	0.40	0.5	0.4245	3.3073	7.2529	0.6309	4.7427	9.9317
		1	0.2192	1.7724	4.0992	0.4531	3.4282	7.2399
		5	0.6086	0.6258	0.6792	0.2294	1.4267	2.4726

thickness and porosity parameters. As it is observed, the porosity parameter contributes to the increase in dimensionless frequencies in FGP beams as the amount of ceramic increases except for the first mode in porosity distribution type III and this parameter shows the significant decreases in dimensionless frequencies in FGP beams as the amount of metal increases. Tables 12-13 display the first three dimensionless critical buckling loads of imperfect FG beams with various boundary conditions and porosity parameters. This parameter has a significant role in predicting buckling responses, the higher values are observed in the ceramic-rich material and decreased to lower magnitudes in the metallic-rich beams, and this difference has grown for higher modes of buckling.

As expected, the FG beams with an increased amount of metal are more susceptible to buckling than ceramic-rich beams, and the porosity parameter contributes to decreasing the dimensionless critical buckling loads as this parameter

Table 13 Benchmark results for first three dimensionless critical buckling loads $\hat{P}_{cr}$ of imperfect FG beams with various boundary conditions and porosity coefficients e_0.(L/h=5)

BCs	e_0	Porosity I			Porosity II		
		1	2	3	1	2	3
CC	0.20	0.0898	0.1321	0.1849	0.0922	0.1335	0.1848
	0.40	0.0893	0.1312	0.1836	0.0950	0.1343	0.1827
	0.60	0.0868	0.1282	0.1800	0.0973	0.1329	0.1767
	0.80	0.0789	0.1190	0.1699	0.0970	0.1256	0.1612
S-S	0.20	0.0296	0.0898	0.1446	0.0309	0.0922	0.1461
	0.40	0.0295	0.0893	0.1437	0.0329	0.0950	0.1468
	0.60	0.0285	0.0868	0.1403	0.0353	0.0973	0.1451
	0.80	0.0253	0.0789	0.1303	0.0383	0.0970	0.1366
C-F	0.20	0.0080	0.0588	0.1190	0.0085	0.0609	0.1210
	0.40	0.0080	0.0585	0.1182	0.0091	0.0637	0.1230
	0.60	0.0077	0.0567	0.1152	0.0100	0.0669	0.1236
	0.80	0.0068	0.0509	0.1059	0.0112	0.0694	0.1192

increases for distribution pattern type I. In contrast to distribution pattern type II, the dimensionless critical buckling loads increase when the porosity parameter increases and provides more resistance.

5. Conclusions

A numerical study of the effect of various porosity distributions on the free vibration and buckling analysis of FGP beams is carried out. The accuracy and efficiency of the formulated two-noded finite element are demonstrated for various porosity distributions, boundary conditions, and material configurations. Based on higher order shear deformation beam theory, the C^0 and C^1 continuities are used to derive the stiffness, geometric, and mass matrices from Hamilton's principle. The present element has only three degrees of freedom per node, and is therefore easier to use than alternate models available in the scientific literature. The shear locking phenomenon is avoided by using the reduced integration technique and without requiring any shear correction factor. The present results have revealed the emergence of several useful conclusions:

- The formulated finite element model captures the effect of porosity distribution on free vibration and buckling using an efficient shear deformation beam theory with only three unknowns. This theory takes into account shear deformation, which beam models frequently ignore or underestimate. This helps us understand complex porosity distribution structures.
- The present element is simple, easy to numerically implement, and free from shear locking.
- Unlike other numerical procedures, the formulated element is more stable with respect to the resulting stiffness, geometric, and mass matrices and offers a guideline to develop sets of other finite element models.
- This investigation tested four porosity distribution patterns on free vibration and buckling responses of FGP beams. Complex porosity distributions are becoming more common in engineering applications, and researchers are attempting to make this a major focus. This research helps design more efficient and robust structures by revealing their behaviour.
- The porosity effect has a variable impact on the computed frequencies, depending on the used porosity distributions. In buckling analysis, the porosity shows a clear trend of decreasing critical buckling loads.
- In addition, the material index is more prominent than the porosity parameter in predicting the critical buckling loads.
- The limit of the porosity parameter must be experimentally defined to establish the optimum choice for imperfect functionally graded structural problems.
- The used approach is precise and efficient, and it assesses large structures with complex porosity distributions. This outperforms methods that ignore shear deformation or are computationally expensive.

Finally, the current study can establish a good pathway for future research, including various mechanical behaviours of imperfect FG beams.

References

Akbaş, Ş.D. (2018), "Forced vibration analysis of functionally graded porous deep beams", *Compos. Structs*., **186**, 293-302. https://doi.org/10.1016/j.compstruct.2017.12.013.

Akbaş, Ş.D. (2021), "Dynamic analysis of axially functionally graded porous beams under a moving load", *Steel Compos. Struct.*, **39**(6), 811-821. https://doi.org/10.12989/scs.2021.39.6.811.

Akbaş, Ş.D., Bashiri, A.H., Assie, A.E. and Eltaher, M.A. (2020), "Dynamic analysis of thick beams with functionally graded porous layers and viscoelastic support", *J. Vib. Control*, **27**(13-14), 1644-1655. https://doi.org/10.1177/1077546320947302.

Alnujaie, A., Akbaş, Ş.D., Eltaher, M.A. and Assie, A.E. (2021), "Damped forced vibration analysis of layered functionally graded thick beams with porosity", *Smart Struct. Syst*., **27**(4), 679-689. https://doi.org/10.12989/sss.2021.27.4.679.

Anirudh, B., Ganapathi, M., Anant, C. and Polit, O. (2019), "A comprehensive analysis of porous graphene-reinforced curved beams by finite element approach using higher-order structural theory: Bending, vibration and buckling", *Compos. Structs*., **222**, 110899. https://doi.org/10.1016/j.compstruct.2019.110899.

Avcar, M. (2019), "Free vibration of imperfect sigmoid and power law functionally graded beams", *Steel Compos. Struct.*, **30**(6), 603-615. https://doi.org/10.12989/scs.2019.30.6.603.

Belabed, Z., Selim, M.M., Slimani, O., Taibi, N., Tounsi, A. and Hussain, M. (2021), "An efficient higher order shear deformation theory for free vibration analysis of functionally graded shells", *Steel Compos. Struct.*, **40**(2), 307-321. https://doi.org/10.12989/scs.2021.40.2.307.

Bendaho, B., Belabed, Z., Bourada, M., Benatta, M.A., Bourada, F. and Tounsi, A. (2019), "Assessment of new 2D and quasi-3D nonlocal theories for free vibration analysis of size-dependent functionally graded (FG) nanoplates", *Adv. Nano Res.*, **7**(4), 279-294. https://doi.org/10.12989/anr.2019.7.4.277.

Chen, D., Yang, J. and Kitipornchai, S. (2015), "Elastic buckling and static bending of shear deformable functionally graded porous beam", *Compos. Structs.*, **133**, 54-61. https://doi.org/10.1016/j.compstruct.2015.07.052.

Chen, D., Yang, J. and Kitipornchai, S. (2016), "Free and forced vibrations of shear deformable functionally graded porous beams", *Int. J. Mech. Sci.*, **108-109**, 14-22. https://doi.org/10.1016/j.ijmecsci.2016.01.025.

Chen, X., Chen, L. and Lu, Y. (2021), "Imperfection sensitivity of nonlinear primary resonance behavior in bi-directional functionally graded porous material beam", *Compos. Structs.*, **271**, 114142. https://doi.org/10.1016/j.compstruct.2021.114142.

Civalek, O. and Avcar, M. (2020), "Free vibration and buckling analyses of CNT reinforced laminated non-rectangular plates by discrete singular convolution method", *Eng. Comput.*, **38**(Suppl 1), 489-521. https://doi.org/10.1007/s00366-020-01168-8.

Cuong-Le, T., Nguyen, K.D., Nguyen-Trong, N., Khatir, S., Nguyen-Xuan, H. and Abdel-Wahab, M. (2020a), "A three-dimensional solution for free vibration and buckling of annular plate, conical, cylinder and cylindrical shell of FG porous-cellular materials using IGA", *Compos. Structs.*, **259**, 113216. https://doi.org/10.1016/j.compstruct.2020.113216.

Cuong-Le, T., Nguyen, T.N., Vu, T.H., Khatir, S. and Abdel Wahab, M. (2020b), "A geometrically nonlinear size-dependent hypothesis for porous functionally graded micro-plate", *Eng. Comput.*, **38**, 449-460. https://doi.org/10.1007/s00366-020-01154-0.

Derikvand, M., Farhatnia, F. and Hodges, D.H. (2021), "Functionally graded thick sandwich beams with porous core: Buckling analysis via differential transform method", *Mech. Base. Des. Struct. Mach.*, 1-28. https://doi.org/10.1080/15397734.2021.1931309.

Dhatt, G., Lefrancois, E. and Touzot, G. (2012), *Finite Element Method*, ISTE Ltd and John Wiley & Sons Inc.

Ebrahimi, F. and Dabbagh, A. (2019), "A novel porosity-based homogenization scheme for propagation of waves in axially-excited FG nanobeams", *Adv. Nano Res.*, **7**(6), 379-390. https://doi.org/10.12989/anr.2019.7.6.379.

Ebrahimi, F. and Zia, M. (2015), "Large amplitude nonlinear vibration analysis of functionally graded Timoshenko beams with porosities", *Acta Astronaut.*, **116**, 117-125. https://doi.org/10.1016/j.actaastro.2015.06.014.

Eltaher, M.A. and Mohamed, S.A. (2020), "Buckling and stability analysis of sandwich beams subjected to varying axial loads", *Steel Compos. Struct.*, **34**(2), 241-260. https://doi.org/10.12989/scs.2020.34.2.241.

Eltaher, M.A., Fouda, N., El-midany, T. and Sadoun, A.M. (2018), "Modified porosity model in analysis of functionally graded porous nanobeams", *J. Brazil. Soc. Mech. Sci. Eng.*, **40**(3), 1-10. https://doi.org/10.1007/s40430-018-1065-0.

Fahsi, B., Bouiadjra, R.B., Mahmoudi, A., Benyoucef, S. and Tounsi, A. (2019), "Assessing the effects of porosity on the bending, buckling, and vibrations of functionally graded beams resting on an elastic foundation by using a new refined Quasi-3D theory", *Mech. Compos. Mater.*, **55**(2), 219-230. https://doi.org/10.1007/s11029-019-09805-0.

Fang, W., Yu, T., Van Lich, L. and Bui, T.Q. (2019), "Analysis of thick porous beams by a quasi-3D theory and isogeometric analysis", *Compos. Structs.*, **221**, 110890. https://doi.org/10.1016/j.compstruct.2019.04.062.

Fazzolari, F.A. (2018), "Generalized exponential, polynomial and trigonometric theories for vibration and stability analysis of porous FG sandwich beams resting on elastic foundations", *Compos. Part B: Eng.*, **136**, 254-271. https://doi.org/10.1016/j.compositesb.2017.10.022.

Galeban, M.R., Mojahedin, A., Taghavi, Y. and Jabbari, M. (2016), "Free vibration of functionally graded thin beams made of saturated porous materials", *Steel Compos. Struct.*, **21**(5), 999-1016. https://doi.org/10.12989/scs.2016.21.5.999.

Gao, K., Li, R. and Yang, J. (2019), "Dynamic characteristics of functionally graded porous beams with interval material properties", *Eng. Struct.*, **197**, 109441. https://doi.org/10.1016/j.engstruct.2019.109441.

Hadji, L. (2020), "Influence of the distribution shape of porosity on the bending of FGM beam using a new higher order shear deformation model", *Smart Struct. Syst.*, **26**(2), 253-262. https://doi.org/10.12989/sss.2020.26.2.253.

Hamed, M.A., Sadoun, A.M. and Eltaher, M.A. (2019), "Effects of porosity models on static behavior of size dependent functionally graded beam", *Struct. Eng. Mech.*, **71**(1), 89-98. https://doi.org/10.12989/sem.2019.71.1.089.

Jamshidi, M., Arghavani, J. and Maboudi, G. (2019), "Post-buckling optimization of two-dimensional functionally graded porous beams", *Int. J. Mech. Mater. Des.*, **15**(4), 801-815. https://doi.org/10.1007/s10999-019-09443-3.

Jena, S.K., Chakraverty, S. and Malikan, M. (2020), "Application of shifted Chebyshev polynomial-based Rayleigh-Ritz method and Navier's technique for vibration analysis of a functionally graded porous beam embedded in Kerr foundation", *Eng. Comput.*, **37**, 3569-3589. https://doi.org/10.1007/s00366-020-01018-7.

Kitipornchai, S., Chen, D. and Yang, J. (2017), "Free vibration and elastic buckling of functionally graded porous beams reinforced by graphene platelets", *Mater. Des.*, **116**, 656-665. https://doi.org/10.1016/j.matdes.2016.12.061.

Li, S.R. and Batra, R.C. (2013), "Relations between buckling loads of functionally graded Timoshenko and homogeneous Euler-Bernoulli beams", *Compos. Struct.*, **95**, 5-9. https://doi.org/10.1016/j.compstruct.2012.07.027.

Liu, T., Guessasma, S., Zhu, J., Zhang, W. and Belhabib, S. (2018), "Functionally graded materials from topology optimisation and stereolithography", *Eur. Polym. J.*, **108**, 199-211. https://doi.org/10.1016/j.eurpolymj.2018.08.038.

Liu, Y., Su, S., Huang, H. and Liang, Y. (2019), "Thermal-mechanical coupling buckling analysis of porous functionally graded sandwich beams based on physical neutral plane", *Compos. Part B: Eng.*, **168**, 236-242. https://doi.org/10.1016/j.compositesb.2018.12.063.

Madenci, E. (2019), "A refined functional and mixed formulation to static analyses of fgm beams", *Struct. Eng. Mech.*, **69**(4), 427-437. https://doi.org/10.12989/sem.2019.69.4.427.

Madenci, E. (2021a), "Free vibration and static analyses of metal-ceramic FG beams via high-order variational MFEM", *Steel Compos. Struct.*, **39**(5), 493-509. https://doi.org/10.12989/scs.2021.39.5.493.

Madenci, E. (2021b), "Free vibration analysis of carbon nanotube RC nanobeams with variational approaches", *Adv. Nano Res.*, **11**(2), 157-171. http://doi.org/10.12989/anr.2021.11.2.157.

Madenci, E. and Gulcu, S. (2020b), "Optimization of flexure stiffness of FGM beams via artificial neural networks by mixed FEM", *Struct. Eng. Mech.*, **75**(5), 633-642. https://doi.org/10.12989/sem.2020.75.5.633.

Madenci, E. and Ozutok, A. (2017), "Variational approximate and mixed-finite element solution for static analysis of laminated

composite plates", *Solid State Phenom.*, **267**, 35-39. https://doi.org/10.4028/www.scientific.net/SSP.267.35.

Madenci, E. and Özütok, A. (2020a), "Variational approximate for high order bending analysis of laminated composite plates", *Struct. Eng. Mech.*, **73**(1), 97-108. http://doi.org/10.12989/sem.2020.73.1.097.

Mehala, T., Belabed, Z., Tounsi, A. and Beg, O.A. (2018). "Investigation of influence of homogenization models on stability and dynamic of FGM plates on elastic foundations", *Geomech. Eng.*, **16**(3), 257-271. http://doi.org/10.12989/gae.2018.16.3.257.

Mehar, K. and Panda, S.K. (2019), "Multiscale modeling approach for thermal buckling analysis of nanocomposite curved structure", *Adv. Nano Res.*, **7**(3), 181-190. https://doi.org/10.12989/anr.2019.7.3.181.

Mirjavadi, S.S., Forsat, M., Yahya, Y.Z., Barati, M.R., Jayasimha, A.N. and Hamouda, A. (2020), "Porosity effects on post-buckling behavior of geometrically imperfect metal foam doubly-curved shells with stiffeners", *Struct. Eng. Mech.*, **75**(6), 701-711. https://doi.org/10.12989/sem.2020.75.6.701.

Mirjavadi, S.S., Mohasel Afshari, B., Khezel, M., Shafiei, N., Rabby, S. and Kordnejad, M. (2018), "Nonlinear vibration and buckling of functionally graded porous nanoscaled beams", *J. Brazil. Soc. Mech. Sci. Eng.*, **40**(7). https://doi.org/10.1007/s40430-018-1272-8.

Nguyen, T.K., Truong-Phong Nguyen, T., Vo, T.P. and Thai, H.T. (2015), "Vibration and buckling analysis of functionally graded sandwich beams by a new higher-order shear deformation theory", *Compos. Part B: Eng.*, **76**, 273-285. https://doi.org/10.1016/j.compositesb.2015.02.032.

Noori, A.R., Aslan, T.A. and Temel, B. (2021), "Dynamic analysis of functionally graded porous beams using complementary functions method in the laplace domain", *Compos. Struct.*, **256**, 113094. https://doi.org/10.1016/j.compstruct.2020.113094.

Özütok, A. and Madenci, E. (2017), "Static analysis of laminated composite beams based on higher-order shear deformation theory by using mixed-type finite element method", *Int. J. Mech. Sci.*, **130**, 234-243. https://doi.org/10.1016/j.ijmecsci.2017.06.013.

Punera, D. and Kant, T. (2019), "A critical review of stress and vibration analyses of functionally graded shell structures", *Compos. Struct.*, **210**, 787-809. https://doi.org/10.1016/j.compstruct.2018.11.084.

Qin, B., Zhong, R., Wang, Q. and Zhao, X. (2020), "A Jacobi-Ritz approach for FGP beams with arbitrary boundary conditions based on a higher-order shear deformation theory", *Compos. Struct.*, **247**, 112435. https://doi.org/10.1016/j.compstruct.2020.112435.

Reddy, J.N. (2004), *Mechanics of Laminated Composite Plates and Shells: Theory and Analysis*, 2nd Edition, CRC Press.

Selmi, A. (2020), "Exact solution for nonlinear vibration of clamped-clamped functionally graded buckled beam", *Smart Struct. Syst.*, **26**(3), 361-371. https://doi.org/10.12989/sss.2020.26.3.361.

Şimşek, M. (2010), "Fundamental frequency analysis of functionally graded beams by using different higher-order beam theories", *Nucl. Eng. Des.*, **240**(4), 697-705. https://doi.org/10.1016/j.nucengdes.2009.12.013.

Slimani, O., Belabed, Z., Hammadi, F., Taibi, N. and Tounsi, A. (2021), "A new shear deformation shell theory for free vibration analysis of FG sandwich shells", *Struct. Eng. Mech.*, **78**(6), 739-753. https://doi.org/10.12989/sem.2021.78.6.739.

Smith, B.H., Szyniszewski, S., Hajjar, J.F., Schafer, B.W. and Arwade, S.R. (2012), "Steel foam for structures: A review of applications, manufacturing and material properties", *J. Constr. Steel Res.*, **71**, 1-10. https://doi.org/10.1016/j.jcsr.2011.10.028.

Vinyas, M., Harursampath, D. and Kattimani, S.C. (2021), "On vibration analysis of functionally graded carbon nanotube reinforced magneto-electro-elastic plates with different electro-magnetic conditions using higher order finite element methods", *Def. Technol.*, **17**(1), 287-303. https://doi.org/10.1016/j.dt.2020.03.012.

Vo, T.P., Thai, H.T., Nguyen, T.K., Maheri, A. and Lee, J. (2014), "Finite element model for vibration and buckling of functionally graded sandwich beams based on a refined shear deformation theory", *Eng. Struct.*, **64**, 12-22. https://doi.org/10.1016/j.engstruct.2014.01.029.

Wang, Y.Q. and Zu, J.W. (2017), "Vibration behaviors of functionally graded rectangular plates with porosities and moving in thermal environment", *Aerosp. Sci. Technol.*, **69**, 550-562. https://doi.org/10.1016/j.ast.2017.07.023.

Wattanasakulpong, N., Chaikittiratana, A. and Pornpeerakeat, S. (2018), "Chebyshev collocation approach for vibration analysis of functionally graded porous beams based on third-order shear deformation theory", *Acta Mechanica Sinica*, **34**(6), 1124-1135. https://doi.org/10.1007/s10409-018-0770-3.

Wu, D., Liu, A., Huang, Y., Huang, Y., Pi, Y. and Gao, W. (2018), "Dynamic analysis of functionally graded porous structures through finite element analysis", *Eng. Struct.*, **165**, 287-301. https://doi.org/10.1016/j.engstruct.2018.03.023.

Wu, H., Yang, J. and Kitipornchai, S. (2020), "Mechanical analysis of functionally graded porous structures: A review", *Int. J. Struct. Stab. Dyn.*, **20**(13), 2041015. https://doi.org/10.1142/s0219455420410151.

Xiao, W.S., Gao, Y. and Zhu, H. (2018), "Buckling and post-buckling of magneto-electro-thermo-elastic functionally graded porous nanobeams", *Microsyst. Technol.*, **25**(6), 2451-2470. https://doi.org/10.1007/s00542-018-4145-2.

Xu, Z., Zhang, Z., Wang, J., Chen, X. and Huang, Q. (2020), "Acoustic analysis of functionally graded porous graphene reinforced nanocomposite plates based on a simple quasi-3D HSDT", *Thin Wall. Struct.*, **157**, 107151. https://doi.org/10.1016/j.tws.2020.107151.

Yaylaci, M. and Avcar, M. (2020), "Finite element modeling of contact between an elastic layer and two elastic quarter planes", *Comput. Concrete*, **26**(2), 107-114. https://doi.org/10.12989/cac.2020.26.2.107.

Zahedinejad, P., Zhang, C., Zhang, H. and Ju, S. (2020), "A comprehensive review on vibration analysis of functionally graded beams", *Int. J. Struct. Stab. Dyn.*, **20**(04), 2030002. https://doi.org/10.1142/s0219455420300025.

Zhao, C.Y. (2012), "Review on thermal transport in high porosity cellular metal foams with open cells", *Int. J. Heat Mass Transf.*, **55**(13-14), 3618-3632. https://doi.org/10.1016/j.ijheatmasstransfer.2012.03.017.

Zhao, J., Wang, Q., Deng, X., Choe, K., Xie, F. and Shuai, C. (2019), "A modified series solution for free vibration analyses of moderately thick functionally graded porous (FGP) deep curved and straight beams", *Compos Part B: Eng.*, **165**, 155-166. https://doi.org/10.1016/j.compositesb.2018.11.080.

Zhao, J., Xie, F., Wang, A., Shuai, C., Tang, J. and Wang, Q. (2019), "Vibration behavior of the functionally graded porous (FGP) doubly-curved panels and shells of revolution by using a semi-analytical method", *Compos. Part B-Eng.*, **157**, 219-238. https://doi.org/10.1016/j.compositesb.2018.08.087.

CC